Biophysical Journal Volume 109 December 2015 2602–2613

Article

High-Affinity Interaction of the K-Ras4B Hypervariable Region with the Ras Active Site

Tanmay S. Chavan,[1,2] Hyunbum Jang,[4,5] Lyuba Khavrutskii,[4,5] Sherwin J. Abraham,[2] Avik Banerjee,[3,6] Benjamin C. Freed,[5] Liv Johannessen,[5] Sergey G. Tarasov,[3,6] Vadim Gaponenko,[2,*] Ruth Nussinov,[4,5,7,*] and Nadya I. Tarasova[5,*]

[1]Medicinal Chemistry Department, [2]Biochemistry and Molecular Genetics Department, and [3]Chemistry Department, University of Illinois at Chicago, Chicago, Illinois; [4]Basic Science Program, Leidos Biomedical Research, Inc., Frederick National Laboratory for Cancer Research, [5]Cancer and Inflammation Program, and [6]Structural Biophysics Laboratory, National Cancer Institute at Frederick, Frederick, Maryland; and [7]Department of Human Molecular Genetics and Biochemistry, Sackler School of Medicine, Tel Aviv University, Tel Aviv, Israel

ABSTRACT Ras proteins are small GTPases that act as signal transducers between cell surface receptors and several intracellular signaling cascades. They contain highly homologous catalytic domains and flexible C-terminal hypervariable regions (HVRs) that differ across Ras isoforms. *KRAS* is among the most frequently mutated oncogenes in human tumors. Surprisingly, we found that the C-terminal HVR of K-Ras4B, thought to minimally impact the catalytic domain, directly interacts with the active site of the protein. The interaction is almost 100-fold tighter with the GDP-bound than the GTP-bound protein. HVR binding interferes with Ras-Raf interaction, modulates binding to phospholipids, and slightly slows down nucleotide exchange. The data indicate that contrary to previously suggested models of K-Ras4B signaling, HVR plays essential roles in regulation of signaling. High affinity binding of short peptide analogs of HVR to K-Ras active site suggests that targeting this surface with inhibitory synthetic molecules for the therapy of *KRAS*-dependent tumors is feasible.

INTRODUCTION

K-Ras4B is a ubiquitous p21 GTPase that controls cell survival and proliferation (1). *KRAS* is frequently mutated in cancers of epithelial origin, including lung, colorectal, and pancreatic malignancies (2-4). Oncogenic mutations in K-Ras impair GTP hydrolysis (5) and lead to constitutive activation of signaling (6,7). Despite the central role of K-Ras in oncogenesis and widespread efforts to develop Ras-directed anti-cancer therapeutics (8-11), no selective, specific inhibitor of K-Ras is available for clinical use (12-14). This is primarily because its catalytic domain lacks pockets for high affinity small molecule binders (15,16).

There are two alternative K-Ras mRNA splice variants—K-Ras4A and K-Ras4B. They differ in their 25-amino-acid-long C-terminal hypervariable region (HVR) sequences, where the fourth exon of K-Ras4B encodes a lysine-rich region (17,18). Apart from distinct HVRs, Ras proteins are also differentially posttranslationally modified in their HVRs (19). As a result, the differences in the binding of Ras proteins to their binding partners, or the membrane, could be attributed to their HVRs and the different posttranslational modifications (20). Recent studies clearly demonstrate that each Ras isoform functions in a unique way, differing from other Ras proteins in normal physiological processes as well as in pathogenesis (21,22). The positively charged HVR and the posttranslational modifications target K-Ras4B to the plasma membrane, where it initiates signaling events (23). X-ray and nuclear magnetic resonance (NMR) structural studies point to a highly flexible C-terminal tail (24). NMR chemical shift appears to be a useful tool to obtain the preferred conformational states for an unstructured linker (25).

Our studies indicate that the K-Ras4B HVR interacts with the catalytic domain extensively when the catalytic domain is GDP-loaded. However, when the GTP replaces GDP, the HVR has minimal interaction with the catalytic domain, indicating that the HVR is sequestered in the GDP-bound state and released in the GTP-bound state. Remarkably, the interaction surface identified by NMR and modeling overlaps significantly with those involved in some effectors, such as Raf and PI3K binding. Further, the interaction interface is similar, involving Switch I and β2 regions (see the Ras domain and functional sites shown in Fig. 1). Our data indicates that the HVR interaction is

Submitted June 12, 2015, and accepted for publication September 16, 2015.

*Correspondence: vadimg@uic.edu or nussinor@helix.nih.gov or nadya.tarasova@nih.gov

Tanmay S. Chavan, Hyunbum Jang, and Lyuba Khavrutskii contributed equally to this work.

Tanmay S. Chavan's present address is Department of Molecular & Cellular Physiology, Stanford University, Stanford, California.

Sherwin J. Abraham's present address is Department of Molecular & Cellular Physiology, Stanford University, Stanford, California.

Liv Johanessen's present address is Chemical Biology Program, Harvard University, Boston, Massachusetts.

Editor: Jeff Peng.

0006-3495/15/12/2602/12

http://dx.doi.org/10.1016/j.bpj.2015.09.034

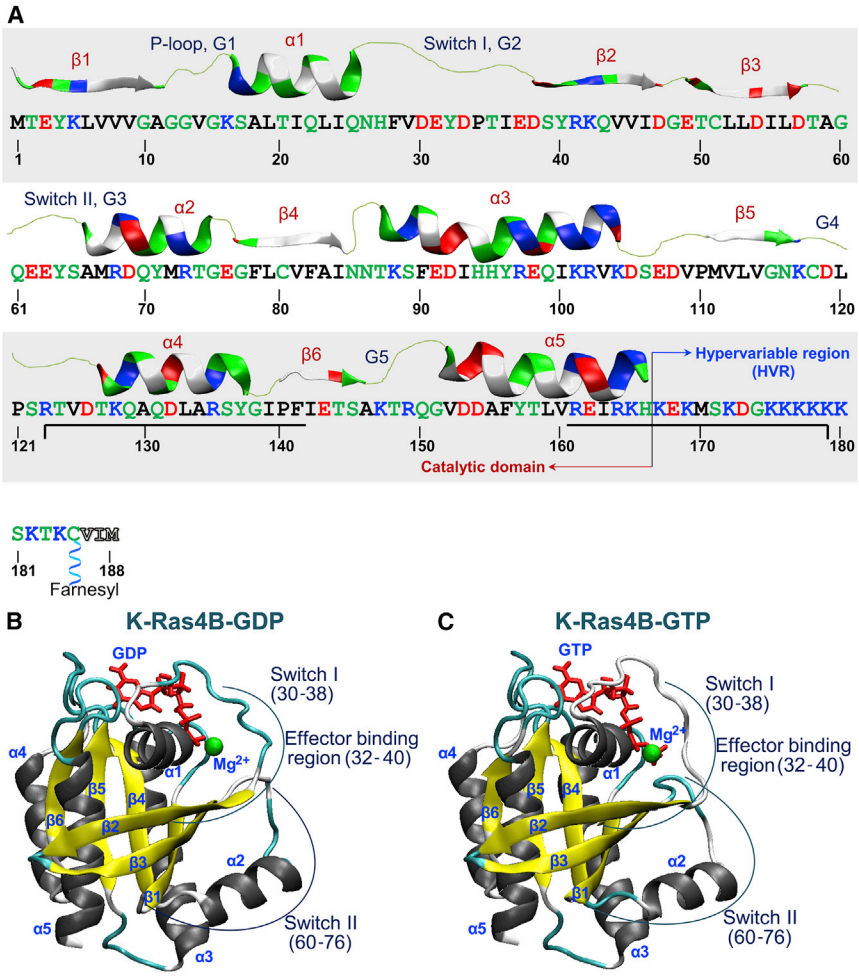

FIGURE 1 K-Ras4B sequence and structures. (*A*) The sequence of the K-Ras4B protein with each domain structure embedded in a cartoon representation. In the sequence are hydrophobic (*black*), polar/glycine (*green*), positively charged (*blue*), and negatively charged (*red*) residues. The same colors were used in the ribbon representation, except for the hydrophobic residues (*white*). Crystal structures of K-Ras4B proteins are in (*B*) GDP-bound (PDB: 4EPT) and (*C*) GTP-bound (PDB: 3GFT) states. The structures were generated for wild-type sequences with the nucleotides modified from the crystalized mutant conformations. In the protein structures, the α-helix (*gray*) and β-sheet (*yellow*) secondary structures are shown. Functional regions are marked on the structures. To see this figure in color, go online.

important in regulation of Ras function. Coupled with membrane interaction and a possible role in orienting and linking membrane-anchored Ras molecules in nanoclusters, HVR emerges as an important player in Ras function in the cell.

MATERIALS AND METHODS

Peptide synthesis

The peptides were synthesized on a Liberty Microwave peptide synthesizer (CEM, Matthews, NC) using Fmoc chemistry. To avoid oxidation, Met residues in the sequence of HVR have been substituted by isosteric norleucine. The peptides were cleaved from the resin and deprotected with a mixture of 90.0% (v/v) TFA (trifluoroacetic acid) with 2.5% water, 2.5% triisopropyl-silane, and 5% thioanisol. The dried crude peptide was dissolved in DMSO (dimethyl sulfoxide) and purified on a preparative (25 × 250 mm) Atlantis C18 reverse phase column (Agilent Technologies, Santa Clara, CA) in a 90 min gradient of 0.1% (v/v) TFA in water and 0.1% TFA in acetonitrile, with a 10 mL/min flow rate. The fractions containing peptides were analyzed on a model No. 1100 LC/MS spectrometer (Agilent Technologies) with the use of a Zorbax 300SB-C3 Poroshell column (Agilent Technologies) and a gradient of 5% acetic acid in water and acetonitrile. Fractions that were >95% pure were combined and freeze-dried. For generation of palmitoylated peptide kR-4B-1, Fmoc-Lys (ε-DDE) was coupled manually to PAL AM resin. The DDE group was removed by incubation with an imidazol/hydroxylamine mixture as described in Johannessen et al. (26). Ten-fold molar excess of palmitic acid was dissolved in methylene chloride/*n*-methylpyrrolidone mixture (1:1), mixed with equimolar amounts of HCTU (^{1}H-Benzotriazolium 1-[bis(dimethylamino)methylene]-5chloro-,hexafluorophosphate (1-),3-oxide) and diisopropylethylamine and added to the resin. After overnight incubation, nonreacted amino groups were blocked with acetic anhydride; the resin was washed with *n*-methylpyrrolidone and methylene chloride and dried under the hood. The rest of the peptide synthesis was performed on the synthesizer as described above.

K-Ras labeling with fluorescein

A quantity of 1.6 mg fluoresceine maleimide (Santa Cruz Biotechnology, Santa Cruz, CA) was dissolved in 25 μL DMSO. Five microliters were diluted in 10 μL buffer. The resulting solution was slowly added to 400 μL of 75 μM GDP or GTP-γ-S-loaded K-Ras solution in 100 mM HEPES buffer pH 6.5 containing 5 mM $MgCl_2$ and 50 mM NaCl. Mixtures were incubated overnight at 4°C and filtered through NAP-5 column (GE Healthcare Life Sciences, Marlborough, MA) equilibrated with the reaction buffer. LC/MS showed no traces of the maleimide and complete labeling of intact K-Ras.

Microscale thermophoresis

For the microscale thermophoresis (MST) studies we have prepared 16 twofold serial dilutions of peptides starting from 30 μM. Titration series

have been prepared that contained 15 μL of 80 nM fluorescein-labeled K-Ras and 15 μL of peptides solution of varying concentrations. Final buffer composition included 20 mM HEPES pH 7.0, 1 mM $MgCl_2$, 0.5 mM TCEP-HCl, 0.5 mM NaN_3, and 10 μM either GDP or GTP-γ-S (Ras buffer) and 0.05% TWEEN-20 for nonlipidated HVR analogs. Lipidated HVR analog kR-4B-1 was dissolved in Ras buffer containing nanodisks composed of 95% DPPC (1,2-dipalmitoyl-*sn*-glycero-3-phosphocholine), and 5% DPPE (1,2-dihexadecanoyl-*sn*-glycero-3-phosphoethanolamine). Nanodisks have been prepared as described in Abraham et al. (27). All measurements were taken in standard treated capillaries on a Monolith NT.115 instrument (NanoTemper Technologies, Munich, Germany) using 60% infrared laser power and an LED excitation source with $\lambda = 470$ nm. NanoTemper Analysis 1.2.20 software was used to fit the data and to determine the K_D values.

Protein preparations

Protein preparation was carried out according to our previously published protocol (27). K-Ras4B cDNA (full-length and catalytic domain) from Invitrogen, Carlsbad, CA was cloned into the pET42a vector (Novagen, Madison, WI). The restriction sites used were *Nde*I and *Xho*I. A His-tag was introduced to aid protein purification. The plasmid was transformed into BL21AI cells and the cells were grown in M9 medium (28) with shaking at 250 rpm. K-Ras4B is generally expressed by *Escherichia coli* in the inclusion bodies. To increase the fraction of the correctly folded and soluble protein, we stimulated production of osmotic shock chaperones by adding 0.4 M NaCl to the expression media as previously described in Abraham et al. (27). The cells were grown at 37°C until their OD_{600} reached 0.6. Then, the expression of K-Ras4B was induced with 0.2 mM IPTG, 0.2% arabinose, and 2% ethanol. The cells were grown thereon for 24 h at 18°C with shaking at 250 rpm. The cells were harvested by centrifuging and the pellets were stored at −80°C. The pellets were thawed at room temperature before lysis. Lysis was carried out using the B-PER bacterial extraction reagent (Pierce Chemical, Rockford, IL) with addition of 10 mM $MgCl_2$, 50 μg/mL DNaseI, 2 mM PMSF (phenylmethanesulfonyl fluoride), 1–2 tablets of EDTA-free complete (Hoffmann-La Roche, Basel, Switzerland), and 10 mg of lysozyme. Pellets were kept in the lysis buffer with shaking at 200 rpm for 40 min at room temperature. The lysate was centrifuged at 14,000 *g* at 4°C and the supernatant was collected. For extracting the protein from the insoluble fraction, the pellets were resuspended in 10 mM Tris-HCl pH 7.6, 20 mM Na-citrate, 50 mM KCl, 5 mM $MgCl_2$, 0.1 mM GDP, and 2 mM β-mercaptoethanol. The protein pellets were kept in this buffer with shaking at 200 rpm for 40 min at room temperature. The suspension was centrifuged similarly to the first lysate and the supernatant was collected. The cell debris was discarded. The first and second extraction fractions were dialyzed separately against 1× binding buffer (Novagen) containing 10% glycerol for ~12 h. Both supernatants were incubated with the His-Bind resin for 3 h. Washing was done with the His-Bind Wash buffer and elution was carried out using a gradient from 30 mM to 1 M imidazole. The purity of the protein was assessed using sodium dodecyl sulfate-polyacrylamide gel electrophoresis and mass spectrometry. Pure fractions were dialyzed against 25 mM Tris-HCl, pH 7.6, 150 mM NaCl, 5% glycerol, 10 mM $MgCl_2$, 1 mM EDTA, and 1 mM β-mercaptoethanol. For nucleotide loading into the protein, 20 μL of 0.5 M EDTA per 1 mL of protein solution was added and GTP-γ-S or GDP was added to a final concentration of 1 mM. This mixture was incubated at 30°C for 30 min. The reaction was stopped by adding 100 mM $MgCl_2$. The buffer was changed to include the Tris-citrate buffer (50 mM Tris-citrate, pH 6.5, 50 mM NaCl, 5 mM $MgCl_2$, 0.01 mM GDP, and 10 mM β-mercaptoethanol). The efficiency of nucleotide exchange was checked by running nucleotides dissociated from K-Ras4B by EDTA (ethylenediaminetetraacetic acid) treatment on a C18 HPLC column. The GTPase hydrolysis assay was carried out to confirm activity of protein. This has been previously reported by our group (27).

NMR experiments

Avance Spectrometers (Bruker Daltonics, Billerica, MA), 900 Mhz and 600 Mhz, equipped with a cryogenic probe, were used for measuring ^1H-^{15}N HSQC NMR spectra. The proteins were dissolved in 50 mM Tris-citrate, pH 6.5, 50 mM NaCl, 5 mM $MgCl_2$, 10 mM β-mercaptoethanol, 10 mM $CaCl_2$, and 10% ^2H_2O for conducting the experiments. All experiments were carried out at 25°C. NMRPipe software (29) was used for processing and analyzing the data. The chemical shift assignments were taken from the BMRB database (http://www.bmrb.wisc.edu) using the BMRB ID: 17785 and 18529 numbers. The assignments for the HVR were made using HNCA, HNCACB, and CBCACOHN experiments. Lysine to alanine mutants were used to resolve ambiguities in lysine assignments in the HVR. The experiments on GTP-γ-S-loaded K-Ras4B were carried out as soon as possible after loading with the GTP-γ-S nucleotide isoforms to ensure that the nucleotide was not hydrolyzed. The mean chemical shift difference was calculated using the following formula:

$$\Delta\delta_{NH} = \sqrt{\frac{\left(\Delta\delta^1 H_N\right)^2 + \left(\Delta\delta^{15} N\right)^2 \Big/ 25}{2}}.$$

Chemical shift perturbations (CSPs) higher than the sum of the average and 1 SD were considered to be statistically significant. The concentrations of proteins used in each experiment are mentioned in the figure legends.

Molecular dynamics simulations

Two Ras crystal structures (PDB: 4EPT and 3GFT) were used to model the full-length K-Ras4B protein (Fig. 1). The former is GDP-loaded with a point mutation C118S. The latter is GppNHp (a GTP analog)-loaded, with a point mutation Q61H. We extracted the coordinates from both crystal structures and replaced the mutants with the wild-type residues. GppNHp was converted to GTP. The coordinates of Mg^{2+} at the active site were also extracted. Then, we constructed an HVR chain and covalently connected it to H166 with the CHARMM program (30). Interactive molecular dynamics (MD) analysis (31) in a molecular visualization program (VMD) (32) with the NAMD (33) code was used to relocate the HVR onto the catalytic domain based on the NMR CSP results and to preequilibrate the proteins for 5 ns. Four different initial configurations for each GDP- and GTP-bound state of K-Ras4B were generated. The initial configurations of the K-Ras4B proteins were solvated by the modified TIP3P water model (34) and gradually relaxed with the proteins held rigid. The unit cell dimension is 120 $Å^3$ containing almost 180,000 atoms. The systems also contain 50 Na^+, and 5 Mg^{2+}, and 61 Cl^- for the GDP-bound K-Ras4B, but a quantity of 60 Cl^- was added to the GTP-bound protein systems. In the preequilibrium stages, a series of minimization and dynamics cycles were performed with the harmonically restrained proteins. At the final preequilibrium stage, the peptide was gradually relaxed by removing the harmonic restraints through dynamic cycles with the full Ewald electrostatics calculation. In the production runs, the Langevin temperature control was used to maintain the constant temperature at 310 K. Nosé-Hoover Langevin piston pressure control was used to sustain the pressure at 1 atm. For production runs of 100 ns, the NAMD code (33) was employed on the Biowulf cluster at the National Institutes of Health (Bethesda, MD). Averages were taken after 30 ns, discarding initial transient trajectories. Analysis was performed with the CHARMM programming package (30).

Raf-1 Ras binding domain assay

The Raf-1 Ras-binding-domain (RBD) assay was carried out according to the protocol published by Chavan et al. (35) using Raf-1 RBD agarose beads from Millipore (Billerica, MA). The assay was done on GDP- and GTP-bound forms of K-Ras4B in its full length and truncated versions or

lysates of H358 lung cancer cells grown in 25 mm dishes and treated with an HVR analog for different time intervals. ImageJ software was used for analyzing the K-Ras4B amounts on Western blots. The ratio of measured band intensities of K-Ras4B$_{1\text{-}166}$ pulled down with Raf-1 RBD beads to K-Ras4B$_{1\text{-}166}$ alone was normalized to a 100%. The full-length protein band intensities were treated in a manner similar to those of K-Ras4B$_{1\text{-}166}$.

SOS1-catalyzed nucleotide exchange

For the experiment, 40 μL of 0.6 μM K-Ras4B$_{1\text{-}166}$ loaded with MANT-GDP (Invitrogen) (0.3 μM final concentration) in 20 mM HEPES buffer pH 7.0 containing 100 mM NaCl, 0.5mM TCEP (tris(2-carboxyethyl)phosphine), 5 mM $MgCl_2$, 0.5 mM NaN_3, and 0.1 mg/mL BSA (bovine serum albumin) was added to the wells of a black low-binding 384-well plate (Cat. No. 3575; Corning, Rochester, NY). After addition of 10 μL stock solution of peptide or buffer, the reaction was started by addition of 10 μL of SOS1 (Cytoskeleton, Denver, CO) solution with the help of a multichannel pipet to provide final 0.6 μM concentration of the guanine nucleotide exchange factor (GEF). Recording of the fluorescence on a FLUOStar fluorescence plate reader (BMG LABTECH, Cary, NC) started ~10 s after SOS1 addition. The measurements continued every 20 s for 40 min and utilized 370 nm excitation (bandwidth 2–5 nm) and 450 nm emission filters. Each experiment was repeated independently five times. Half-lives were determined using single-exponential decay fit in Prism software.

RESULTS

The HVR interacts with the catalytic domain of K-Ras4B in the GDP-bound state and is released in the GTP-bound state

We previously found that the interaction of calmodulin with the HVR of K-Ras4B is inhibited upon GDP binding (36). This observation led us to hypothesize that the catalytic domain of K-Ras4B in its GDP-bound state might sequester the HVR, making it unavailable for protein-protein interactions. To test the hypothesis that HVR interacts with the rest of K-Ras4B and nucleotide binding plays a role in HVR function, we compared the ^{1}H-^{15}N HSQC NMR spectra of K-Ras4B$_{1\text{-}188}$ and K-Ras4B$_{1\text{-}166}$ in the GDP- and GTP-bound states (Fig. 2, *A* and *C*). Spectral comparison revealed residues with significant CSPs caused by HVR. The residues were mapped on the crystal structures of GDP- and GTP-bound K-Ras catalytic domains (Fig. 2, *B* and *D*). Most of the changes occur in the Switch I and effector binding regions, β2, and in the C-terminal helix, α5. This suggests that in the GDP-bound state, the C-terminal HVR interacts extensively with the catalytic domain. An additional indication of the interaction between the HVR and the GDP-bound catalytic domain is the observation of slow conformational exchange between two different states in K-Ras4B$_{1\text{-}188}$-GDP in the catalytic domain residue G60 and the HVR residue G174. The slow exchange in the G60 position is dependent on the presence of the HVR because only a single peak for G60 is found in the spectrum of truncated K-Ras4B$_{1\text{-}166}$-GDP. The rest of the HVR signals are detected as single peaks, which is possibly indicative of fast exchange. When K-Ras4B is GTP-γ-S bound, only very few changes are observed in the Switch I and effector binding regions (I36) and in the adjacent N-terminal portion (S17 and A18).

To further validate our NMR data, we analyzed the effect of HVR mutations K180A and K182A on the structure of the catalytic domain. We reasoned that any change in the structure of HVR should have an effect on the catalytic domain of K-Ras4B-GDP if the HVR is indeed sequestered by the Switch I region. HVR mutations K180A and K182A caused significant CSPs in the Switch I region of K-Ras4B-GDP. We performed additional ^{15}N HSQC NMR experiments on HVR point mutants, K180A and K182A, in the GDP-bound state. CSPs were obtained by comparing the spectra of the K180A (Fig. 3, *A* and *B*) and K182A (Fig. 3, *C* and *D*) mutants with the spectrum of wild-type K-Ras4B$_{1\text{-}188}$-GDP. We observed significant CSPs in the Switch I region (residues 30–38) and α1 helix (residues 16–26). In both cases, E37 exhibited the highest CSPs, suggesting that these lysine residues are involved in HVR sequestration by the catalytic domain. The K180 and K182 residues are relatively far removed from the HVR attachment to the catalytic domain and are expected to have a reduced effect on HVR sequestration. An HVR mutation in the region closer to the catalytic domain is anticipated to more significantly perturb the chemical shifts in the catalytic domain than the K180A and K182A mutations. To test this hypothesis, we prepared K-Ras4B$_{1\text{-}188}$-GDP bearing a K175A mutation in the HVR (Fig. S1 in the Supporting Material). Comparisons of NMR chemical shift differences between the mutant and wild-type full-length proteins revealed larger and more numerous CSPs caused by the K175A than those caused by the K180A and K182A mutations. These data suggest that the K175A mutation induces a significant disruption of the HVR-catalytic domain interaction.

The recently published crystal structures of K-Ras4B exhibit a helix-5 C-terminal extended by two additional turns (9). This structure suggests that, due to the extended helix-5, it would be difficult for the HVR to reach the effector binding region in the catalytic domain. To address this issue, we analyzed *B*-factors for this part of the molecule (Fig. S2). The *B*-factors for helix-5 are high, suggesting a high degree of flexibility. To address the possibility that the HVR may be flexible, we measured ^{1}H-[^{15}N] heteronuclear nuclear Overhauser effect (NOEs) for K-Ras4B-GDP (Fig. 3 *E*). Most of the structure of the catalytic domain is rigid with heteronuclear NOEs in the range between 0.8 and 1. Residue H166 exhibits a negative heteronuclear NOE, suggesting a high degree of disorder. Residues 167–169 have positive but low heteronuclear NOEs of ~0.5. G174 has a positive but very low heteronuclear NOE of 0.1 and is in a flexible area. The lysines K175, K176, K177, K178, K179, and K180 exhibit positive heteronuclear NOEs approaching 0.8, suggesting a relatively rigid conformation for this part of the molecule. One reason for the

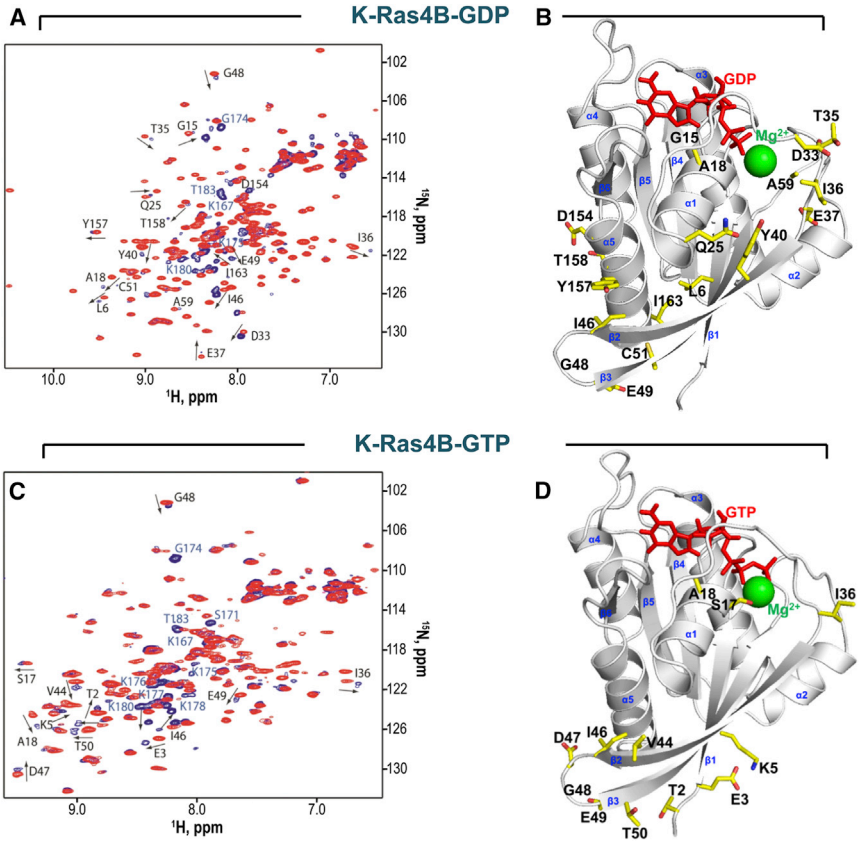

FIGURE 2 NMR CSPs of residues in the full-length and truncated K-Ras4B in the GDP-bound and GTP-bound states by the HVR, and their mapping onto crystal structures. Superimpositions of ^{1}H-^{15}N HSQC spectra of (*A*) full-length K-Ras4B (*blue*, 0.78 mM) and truncated K-Ras4B$_{1\text{-}166}$ (*red*, 1 mM) in the GDP-bound states, and (*B*) mapping of the perturbed residues on the structure of the GDP-bound K-Ras4B catalytic domain; (*C*) full-length K-Ras4B (*blue*, 0.5 mM) and truncated K-Ras4B$_{1\text{-}166}$ (*red*, 0.4 mM) in the GTP-γ-S-bound states, and (*D*) mapping of the perturbed residues on the catalytic domain structure of GTP-bound K-Ras4B. (*Arrows*) Examples of CSPs and their resonance assignments. New resonances in the spectrum of full-length K-Ras4B represent the HVRs (shown in *blue*). In the structures, the side chains of residues with statistically significant CSPs are shown (*yellow*) and marked with residue type and number. These experiments were performed using a 900 Mhz Avance Spectrometer (Bruker Daltonics). To see this figure in color, go online.

increased rigidity is binding of these lysines to the catalytic domain. Residues 181, 182, 183, and 184 have heteronuclear NOEs suggestive of high flexibility.

K-Ras4B HVR analogs interact with K-Ras$_{1\text{-}166}$ with high affinity

High affinity interactions of HVR with the catalytic domain of K-Ras4B are more likely to play a significant functional role than transient low affinity binding. To determine the affinity of HVR for GDP- and GTP-γ-S-loaded K-Ras4B$_{1\text{-}166}$, we generated a K-Ras4B HVR synthetic analog (kR-4B-17: Ac-KEKL$_N$SKDGKKKKKKSKTK-NH$_2$). MST (37,38) revealed that the peptide interacts better with GDP- than with GTP-γ-S-bound K-Ras4B$_{1\text{-}166}$, with dissociation constants, K_D, of 250.0 $\pm$ 33.4 nM and 18.6 $\pm$ 0.9 μM, respectively (Fig. 4 *A*). The interaction appeared sequence-specific. Substitution of just one residue, D173, with proline (kR-4B-28: Ac-KEKL$_N$SKPGKKKKKKSKTK-NH$_2$) abolished the interaction. The D173P mutation was selected because of its likely disruptive effect on any secondary structure elements that might form in the N-terminal portion of the HVR to stabilize its interaction with the catalytic domain. In addition, phosphorylation of S181 (kR-4B-26: Ac-KEKL$_N$ SKDGKKKKKKS(PO$_4$)KTK-NH$_2$), a posttranslational modification known to regulate K-Ras4B interaction with calmodulin (39), prevents binding of HVR to the catalytic domain. To determine whether membrane interaction prevents the HVR from binding the G-domain, we performed binding studies for the lipidated K-Ras4B HVR analog (kR-4B-1: Ac-KEKL$_N$SKDGKKKKKKSKTKK-ε-Pal-NH$_2$) in the presence of membrane-mimicking nanodisks (Fig. 4 *B*). Membrane anchoring of the HVR analog had no significant effects on its interaction with K-Ras4B$_{1\text{-}166}$-GDP (K_D = 230.0 $\pm$ 22.1 nM).

Next, using NMR, we addressed the question of specificity of high affinity peptide binding to the catalytic domain of K-Ras4B-GDP. We added an excess (1.5 molar equivalents) of the HVR peptide to ^{15}N-enriched K-Ras4B$_{1\text{-}166}$-GDP and compared its ^{15}N HSQC spectra with and without the peptide. The results highlight resonances for D30, Y32, I36 and T158, and four side chains (Fig. 5 *A*). The CSPs induced by the HVR in the full-length and truncated proteins concentrate in the same area, namely the Switch I region and helix α5. Moreover, comparison of side-chain resonances in the ε-NH region of the spectra indicates striking similarities between chemical shifts in K-Ras$_{1\text{-}166}$-GDP bound to the HVR peptide and in full-length K-Ras4B-GDP. The similarity of CSPs induced by HVR peptide addition (Fig. 5 *B*) and those induced by HVR in the full-length protein (Fig. 5 *C*) indicates the specificity of HVR to the catalytic domain of K-Ras4B-GDP. To observe the impact of membrane phospholipids on HVR binding to the catalytic domain, we compared ^{1}H-^{15}N HSQC spectra

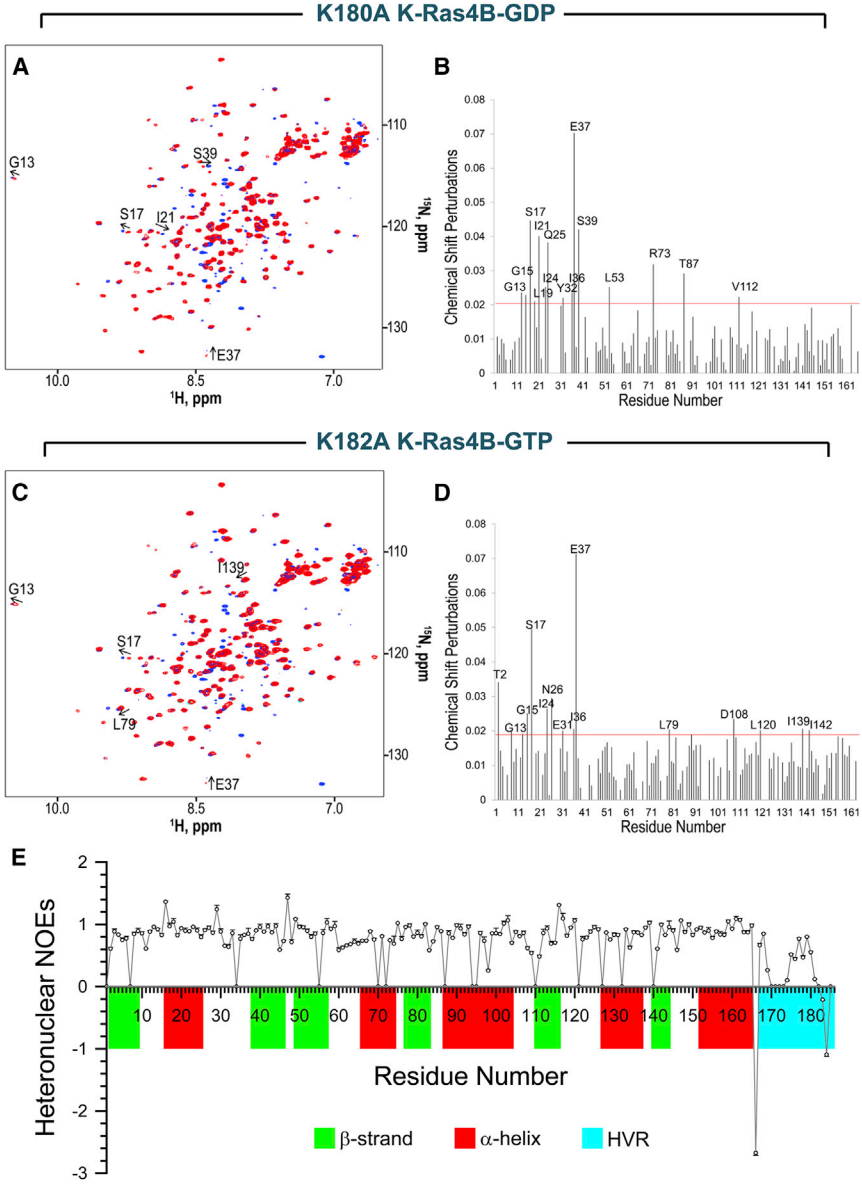

FIGURE 3 CSPs obtained after comparing K-Ras4B-GDP K180A and K182A mutants. Overlays of ^{15}N-HSQC NMR spectra of full-length, wild-type K-Ras4B-GDP protein (*blue*) and (*A*) K180A and (*C*) K182A mutants of K-Ras4B-GDP (*red*). The CSPs measured from the spectra for (*B*) K180A and (*D*) K182A mutants. (*Arrows*) Examples of chemical shift changes. (*Red horizontal line* in the graph) Sum of average CSP with 1 SD. The names of residues exhibiting statistically significant (*above the line*) CSPs are marked. (*E*) ^{1}H-[^{15}N] heteronuclear NOEs for full-length K-Ras4B-GDP. To see this figure in color, go online.

of ^{15}N-enriched K-Ras4B$_{1\text{-}188}$-GDP in the presence and absence of nanodisks (Fig. 5 *D*). We used DPPC nanodisks at the 1:100 (protein/lipid) molar ratio. Our initial hypothesis is that the HVR in K-Ras4B-GDP does not extensively interact with the membrane. Nanodisks induced chemical shift changes in E3, the Switch I region (G12, V29), the effector binding region (D30, S32, E33), Switch II (I46, C51, D54, G60), K147, and the HVR (G174, K175, K176, and K177). While HVR partly participates in K-Ras4B$_{1\text{-}188}$-GDP binding the phospholipids, the catalytic domain is a major contributor. Interestingly, resonances for K178, K179, and K180 did not change upon addition of phospholipids, suggesting that these lysines are not involved in membrane binding when K-Ras4B is in the GDP-bound state. Thus, the membrane only partly competes with the sequestered HVR in K-Ras4B-GDP. In contrast, an overlay of ^{15}N HSQC spectra of K-Ras4B-GTP-γ-S in the presence and absence of DPPC nanodisks shown in Fig. 5 *E* indicates CSPs induced predominantly in the HVR. In addition, binding studies utilizing nanodisks as membrane mimetics have shown that K-Ras4B-GTP-γ-S has a higher affinity for phospholipid bilayers than K-Ras4B-GDP (Fig. S3).

Atomic details of the HVR interaction with the catalytic domain

NMR-based structural determination of full-length K-Ras was difficult due to significant resonance line-broadening caused by conformational exchanges. To obtain structural details of the HVR interaction with the GDP-bound catalytic domain, we performed all-atom MD simulations (30,33) on K-Ras4B$_{1\text{-}185}$ and K-Ras4B$_{1\text{-}166}$ in an aqueous environment.

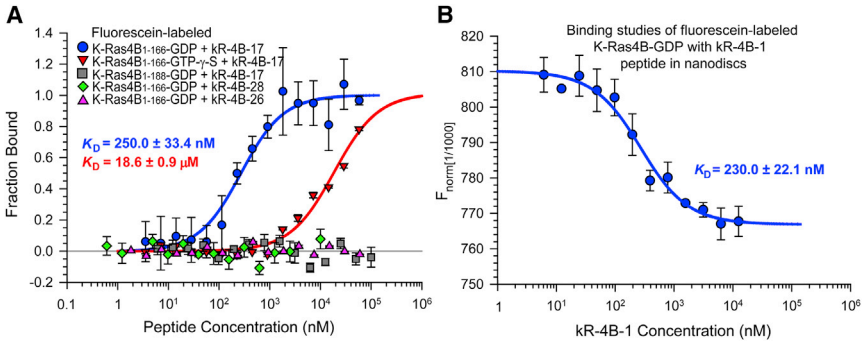

FIGURE 4 Analogs of K-Ras4B HVR interact with recombinant truncated K-Ras4B$_{1\text{-}166}$. (*A*) The interaction was characterized using recombinant K-Ras4B$_{1\text{-}166}$ that was labeled on Cys^{118} with fluorescein maleimide. GDP-bound and GTP-γ-S-bound proteins have been titrated with a synthetic HVR analog, the kR-4B-17 peptide, Ac-KEKL$_N$SKDGKKKKKKSKTK-NH$_2$; its variant kR-4B-28 that had D173P substitution, Ac-KEKL$_N$SKPGKKKKKKSKTK-NH$_2$; and phosphorylated analog kR-4B-26, Ac-KEKL$_N$SKDGKKKKKS(PO$_4$)KTK-NH$_2$. Addition of kR-4B-17, but not of the control or phosphorylated analog, caused a significant change in the protein thermophoretic mobility that allowed for determination of K_D. (*B*) Palmitoylated HVR analog kR-4B-1, Ac-KEKL$_N$SKDGKKKKKKSKTKK-ε-Pal-NH$_2$ showed high affinity binding to GDP-loaded K-Ras4B$_{1\text{-}166}$ in the presence of membrane-mimicking nanodisks. To see this figure in color, go online.

The crystal structures of the GDP- and GTP-bound catalytic domains (Fig. S4 A) were used to generate four different initial configurations based on the NMR CSP data (Fig. S4, B and C). During the initial generation, the HVR chain folded over residues presenting highly perturbed NMR chemical shifts (Fig. 2). Four independent simulations for each nucleotide with the full-length as well as truncated Ras proteins as controls were carried out. Three of the four configurations retain the HVR on the catalytic domain of K-Ras4B-GDP, while only two out of four retain the HVR on K-Ras4B-GTP, marginally interacting with the catalytic domain (Fig. 6). We calculated the interaction energy of the HVR with the catalytic domain to determine the best candidate for the structural model of folded HVR (Fig. S5). The interactions of the HVR with the catalytic domain are mainly driven by electrostatics and reveal stronger attraction in K-Ras4B-GDP as compared to the GTP counterpart. Based on these data, we designated the configurations 2 and 3 of K-Ras4B-GDP and the configurations 3 and 4 of K-Ras4B-GTP as the best model conformations of HVR interacting with the catalytic domain. We speculate that these configurations can reflect sampled ensembles of K-Ras4B conformations in solution for the highly populated NMR observations.

The catalytic domain is highly conserved during the simulations, with root-mean-squared deviation (RMSD) <1.0 Å relative to the starting point for truncated K-Ras4B$_{1\text{-}166}$ (Fig. S6, A and B). For full-length K-Ras4B$_{1\text{-}185}$, although

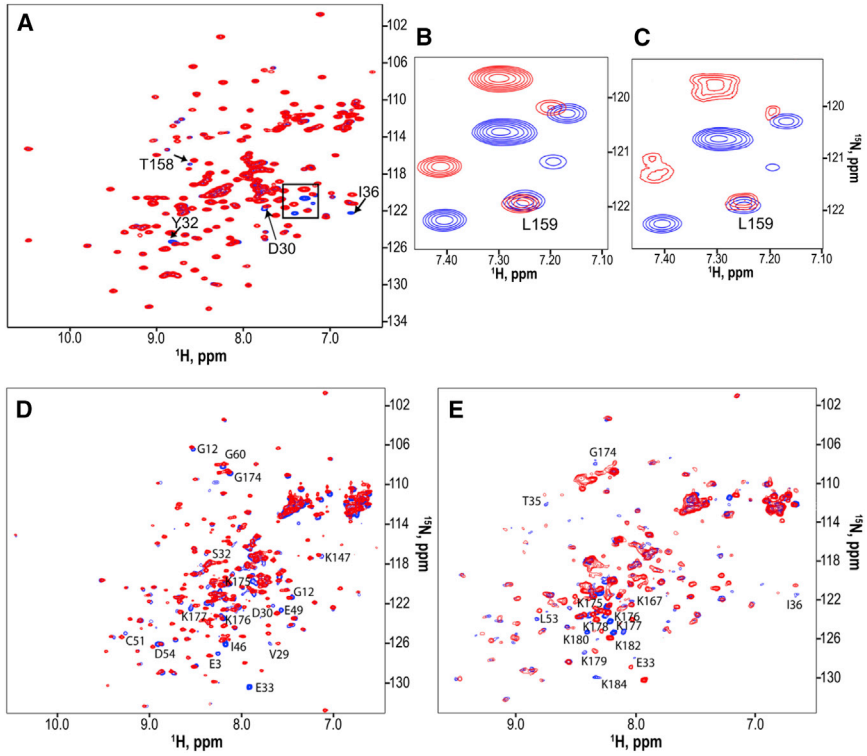

FIGURE 5 Investigation by NMR of interactions of the HVR with the GDP-bound state of the catalytic domain of K-Ras4B. (*A*) A superimposition of ^{15}N HSQC spectra of GDP-bound K-Ras4B$_{1\text{-}166}$ in the absence (*blue*) and in the presence of 1.5 molar equivalents of the HVR peptide (*red*). (*Arrows*) Examples of CSPs. Zoomed-in ε-NH regions in spectral superimpositions of (*B*) GDP-bound K-Ras4B$_{1\text{-}166}$ in the absence (*blue*) and in the presence of 1.5 molar equivalents of the HVR peptide (*red*) and (*C*) full-length GDP-bound K-Ras4B (*red*, 0.4 mM) and GDP-bound K-Ras4B$_{1\text{-}166}$ (*blue*, 1 mM). These experiments were performed using a 600 Mhz Avance Spectrometer (Bruker Daltonics). The chemical shift changes induced by HVR in the full-length protein are more numerous than those caused by the HVR peptide in the catalytic domain of K-Ras4B-GDP. The reason for this may be the higher effective concentration of HVR in the full-length protein, as compared to peptide titration into a solution containing the catalytic domain. Overlays of ^{15}N HSQC spectra of (*D*) 0.4 mM full-length K-Ras4B-GDP (*red*) and 0.4 mM K-Ras4B-GDP in the presence of a 100-fold molar access of DPPC lipids (*blue*) and (*E*) of 0.37 mM full-length K-Ras4B-GTP-γ-S (*red*) and 0.37 mM K-Ras4B-GTP-γ-S in the presence of a 100-fold molar access of DPPC lipids (*blue*). CSPs are marked. To see this figure in color, go online.

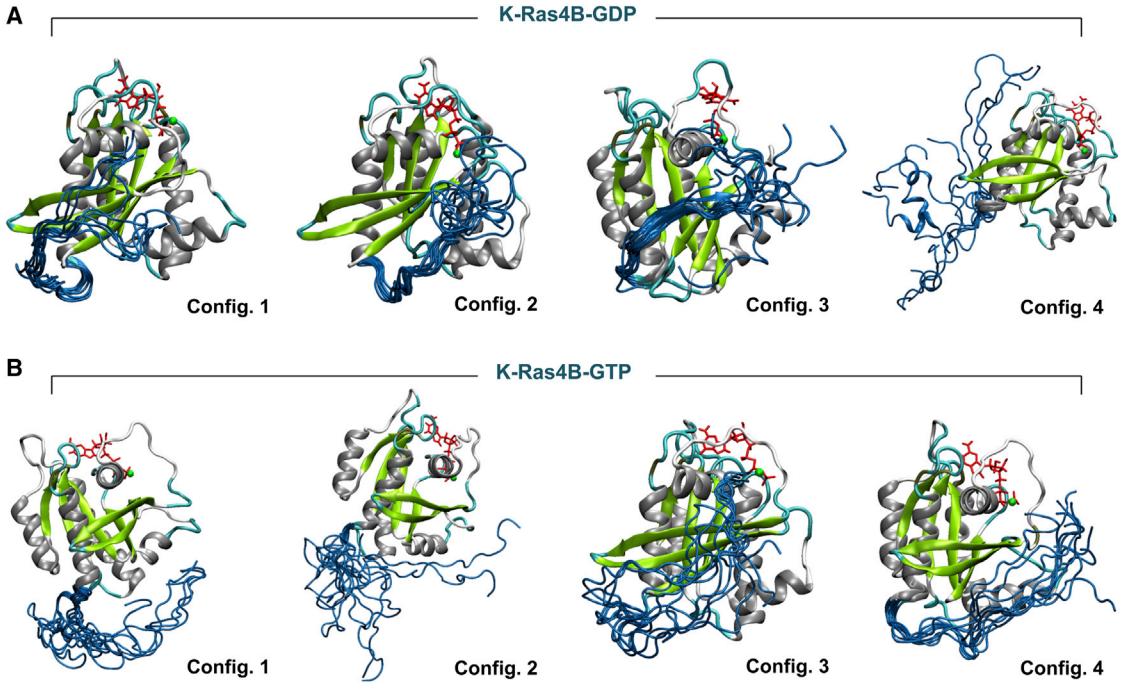

FIGURE 6 Computational modeling of the HVR. Relaxed structures of full-length K-Ras4B in the aqueous environments. Ensembles of HVR structures sampled at each 10 ns simulation are shown on the averaged catalytic domain structures of K-Ras4B over 100 ns MD simulations in the (*A*) GDP-bound and (*B*) GTP-bound states. In the catalytic domain, the α-helix (*gray*) and β-sheet (*yellow*) secondary structures are shown; (*blue*) HVR. To see this figure in color, go online.

the overall conformation of the catalytic domain is preserved with RMSD <1.5 Å, there are subtle structural rearrangements in the effector binding lobe, including Switch I, Switch II, helices α1 and α5, and β1–3 strands in K-Ras4B-GDP, and Switch I, Switch II, and helix α1 in K-Ras4B-GTP (Fig. S6, D and E). Further, large structural differences are observed when the catalytic domains are compared between the full-length GDP- and GTP-bound states, in contrast to the truncated states (Fig. S6, C and F). These differences are expected to favor HVR binding to GDP-bound as compared to GTP-bound Ras. This is in agreement with the NMR and MST data showing that the HVR is sequestered by the catalytic domain in GDP-bound K-Ras4B, but is released in the GTP-bound state. In both GDP- and GTP-bound states, the highly populated HVR conformations are mainly coiled chains (Fig. S7), although a transient β-sheet extended over the β2-strand can be formed by the HVR of configuration 3 of K-Ras4B-GDP (Fig. S8). In the GDP-bound state, the N-terminal portion of the HVR is relatively rigid, attaching tightly to the catalytic domain, while the C-terminal portion of the HVR is rather flexible (Fig. 6). For configuration 2 of K-Ras4B-GDP, the tighter interaction of the coiled HVR with the catalytic domain is likely attributed to salt-bridge formations. This conformation predicts that HVR residues K172 and K175 form salt bridges with E3 and E37, respectively. Other lysines in the polybasic region (residues 175–180) also form salt bridges with D38 in Switch I and E62 and E63 in Switch II regions, strongly sequestrating the HVR to the effector lobe. For configuration 3 of K-Ras4B-GDP, the HVR is observed to populate a β-sheet with higher occupancy of a β-strand conformation in the S171- D173 region, forming an antiparallel β-sheet motif. HVR residue D173 forms a salt bridge with K42, stabilizing the HVR β-sheet. The polybasic lysines also form salt bridges with E37, D38, and D54. Lateral shifts in the HVR β-strand location are possible. Although the upstream-terminal portions of both coiled and stranded HVRs interact with different regions of catalytic domain, their polybasic lysines commonly interact with the Switch I and β2 regions. This β2-strand is in the effector interaction site, with the HVR antiparallel β-sheet mimicking the common Ras effector-binding motif. To complement the NMR CSPs, we calculated the combined CSPs (40,41), mapping them over K-Ras4B$_{1\text{-}166}$ (Fig. S9, A and B). In the GDP-bound state, many residues exhibit perturbations, especially in the Switch I and effector binding regions, in agreement with the NMR results (Fig. S9, C and D). In the GTP-bound state, fewer residues are perturbed, suggesting loose HVR-catalytic domain interaction. Perturbations of thermal fluctuations during the simulations for K-Ras4B with respect to K-Ras4B$_{1\text{-}166}$ also point to residues in β2, including the effector-binding region and Switch I and II, as HVR binding sites (Fig. S9, E and F). Interactions between the HVR and the GDP-bound catalytic domain are transient, suggesting that multiple possible modes of interactions are common. NMR experiments and computational analysis were done

in the absence of C-terminal lipidation, while one HVR peptide was modified with a lipid group for binding affinity studies, which suggests a stable association.

The interaction of HVR with the catalytic domain prevents low affinity Raf1 binding to K-Ras4B-GDP but has a small effect on GEF-catalyzed nucleotide exchange

Ras-dependent activation of Raf-1 is initiated when its Ras-binding domain (Raf-1 RBD) interacts with the effector region of Ras-GTP with nanomolar affinity. Raf-1 also binds to Ras-GDP with an affinity that is 100-fold lower than that for Ras-GTP (42). The low affinity binding to Ras-GDP may be relevant in cells because in the full-length Raf-1 protein, the cysteine-rich domain also binds Ras in a nucleotide-independent manner (43). The HVR interacts with the catalytic domain through the effector binding site. To investigate the impact of HVR sequestration on Raf-1 interaction, we performed the Raf-1 binding assay (35) with the full-length and truncated forms of K-Ras4B-GTP-γ-S and K-Ras4B-GDP. The comparison of Raf-1 binding was done with K-Ras4B$_{1\text{-}166}$-GTP-γ-S against K-Ras4B$_{1\text{-}188}$-GTP-γ-S and with K-Ras4B$_{1\text{-}166}$-GDP against K-Ras4B$_{1\text{-}188}$-GDP (Fig. 7 *A*). Our results demonstrate that full-length K-Ras4B-GDP binds Raf-1 RBD with 52% efficiency when compared to the catalytic domain of K-Ras4B-GDP. The low efficiency of Raf RBD binding to K-Ras4B$_{1\text{-}188}$-GDP compared to K-Ras4B$_{1\text{-}166}$-GDP suggests that the HVR interferes with the effector binding to the catalytic domain. At the same time, we observed an ~27% increase in the efficiency of Raf-1 RBD binding to GTP-γ-S loaded full-length K-Ras4B compared to the catalytic domain, suggesting that the HVR can interact with Raf. Thus, our findings suggest that K-Ras4B in the GDP-bound state is autoinhibited by its HVR. To address the question of whether autoinhibited K-Ras4B can be activated by GEFs, we evaluated the influence of HVR analogs on nucleotide exchange catalyzed by the GEF SOS1 using K-Ras4B$_{1\text{-}166}$ loaded with the fluorogenic GDP analog MANT-GDP. The addition of 570 nM synthetic HVR analog increased the half-time ($T_{1/2}$) of the SOS1-catalyzed nucleotide exchange from 590 $\pm$ 20 s to 780 $\pm$ 25 s. (Fig. 7 *B*). Further increase in the HVR analog concentration up to 14 μM did not improve the degree of nucleotide exchange inhibition, suggesting that the modest decrease in exchange rate by 35% was the maximal achievable effect under the conditions used. Our results demonstrate that the autoinhibited form of K-Ras4B can be activated by a GEF, albeit to a lesser extent than K-Ras4B without its HVR. The overlap in the HVR binding interface of K-Ras4B with that of GEFs is significantly lesser than with Raf. For the modeled Ras/effector complexes reconstituted from the crystal structures, the overlapped surface areas in the HVR binding interface by the effectors are 332.7 Å^2 and 289.1 Å^2 for the Raf and GEF, respectively (Fig. S10). Consistent with the little direct overlap in binding surfaces, HVR has only a moderate effect on nucleotide exchange. It is important to note that HVR sequestration does not permanently inhibit K-Ras4B, because it does not prevent its activation by GEFs. The autoinhibited state can be reversed upon proper stimulation.

DISCUSSION

The paradigm for Ras function states that resting GDP-bound Ras is activated by GEFs catalyzing GDP exchange for GTP (44). GTP binding induces a conformational change in the Switch I and Switch II regions and exposes the effector interaction site in Ras (45). Ras effectors, such as Raf kinase, bind Ras-GTP with a higher affinity than Ras-GDP and this allows initiation of signaling. Signaling proceeds until Ras hydrolyzes GTP to GDP with the help of GTPase activating proteins. Subsequently, the low affinity effector-Ras-GDP complex dissociates and signaling stops. Our results suggest that this model of Ras function is incomplete. We show that HVR is sequestered by the GDP-bound catalytic domain of K-Ras4B but is released in the GTP-bound state. We propose that GDP-bound K-Ras4B is autoinhibited by its HVR, which dictates how K-Ras4B is activated, how it is recruited to the plasma membrane, and how K-Ras4B signaling is initiated and stopped after GTP hydrolysis. The structural details of the HVR interaction with the catalytic domain in the GDP-bound states from the simulations illustrate that the HVR prefers to interact with the effector binding site in the effector lobe of the protein. Similarly, the HVR also resides in the effector lobe side in the GTP-bound state, although the HVR marginally interacts with the catalytic domain. The HVR residency on the effector lobe suggests that the HVR may function as a switch through releasing and retaining the HVR autoinhibition.

Autoinhibition by HVR regulates K-Ras4B interactions with the plasma membrane phospholipids. HVR is a major membrane targeting element in Ras GTPases (19). Its sequestration by the GDP-bound catalytic domain reduces the affinity of K-Ras4B for the lipid bilayers (Fig. S3), temporarily discontinuing signaling. A similar nucleotide-dependent mechanism is employed by Arf and Rac GTPases to regulate their function at the plasma membrane (46,47).

Concomitantly, HVR sequestration can regulate effector binding to K-Ras4B. It is remarkable that the K-Ras4B$_{1\text{-}166}$-HVR β-sheet interface is similar to that of Raf RBD. We speculate that within the HVR ensemble, a preexisting β-strand conformer selectively binds to the functional site of the K-Ras4B catalytic domain to extend the β-sheet, a common interface motif. Consistent with this mode of interaction, HVR significantly affects binding of GDP-loaded K-Ras4B to Raf RBD. The markedly less effective binding of Raf RBD to GDP-bound K-Ras4B$_{1\text{-}188}$ than to GDP-bound K-Ras4B$_{1\text{-}166}$ suggests that the HVR plays an important

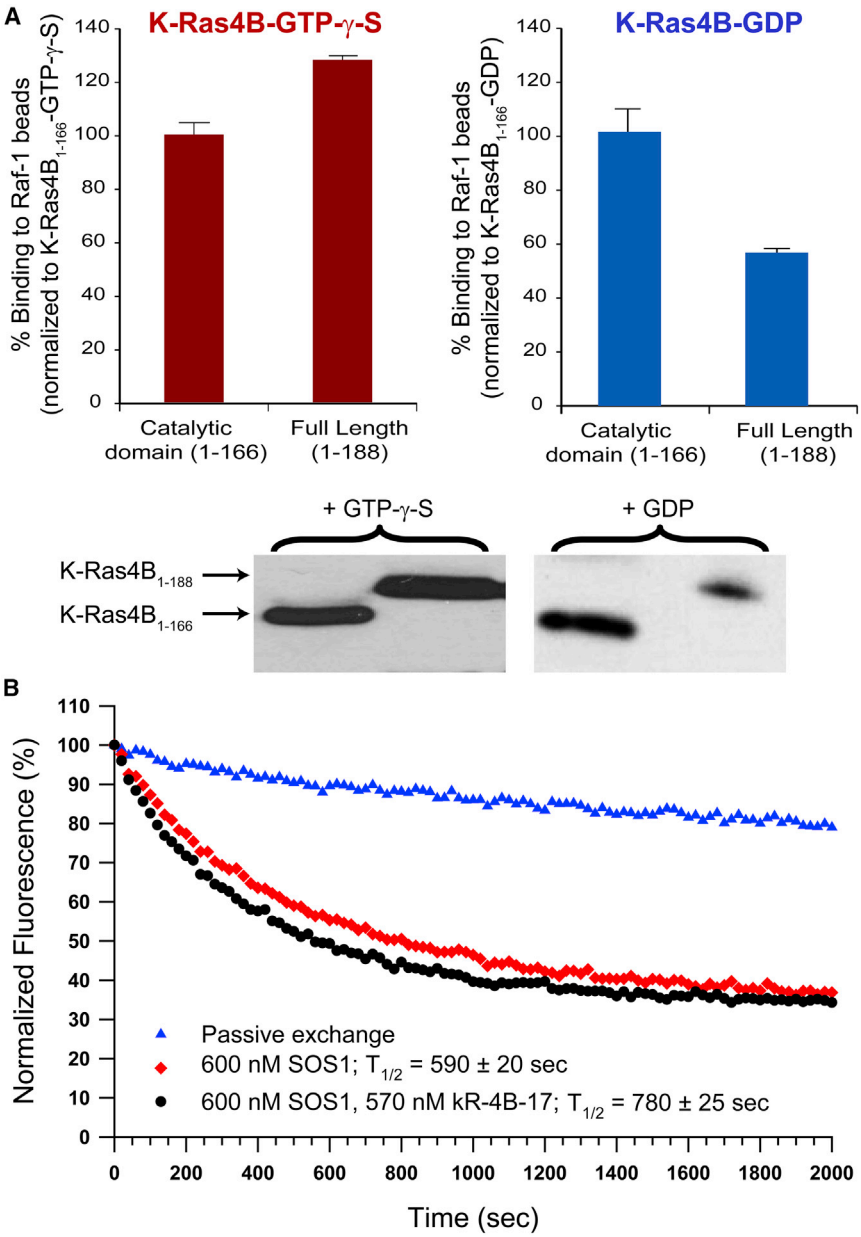

FIGURE 7 HVR binding to the catalytic domain reduces the interaction of Raf-1RBD with full-length K-Ras4B-GDP but not with K-Ras4B-GTP-γ-S and moderately interferes with nucleotide exchange. (*A*) An RBD pull-down assay was used to determine the difference in binding of equal amounts of the catalytic domain and full-length K-Ras4B in its GTP-γ-S and GDP-bound states. The amount of Raf-1 RBD bound to either K-Ras4B$_{1\text{-}166}$-GTP-γ-S or K-Ras4B$_{1\text{-}166}$-GDP was assumed to be 100%. Thus, RBD binding of full-length K-Ras4B$_{1\text{-}188}$-GTP-γ-S was 127.8 ± 2% when normalized to K-Ras4B$_{1\text{-}166}$-GTP-γ-S binding. However, RBD binding of K-Ras4B$_{1\text{-}188}$-GDP was only 55.2 ± 3.1% when compared to K-Ras4B$_{1\text{-}166}$-GDP binding. Thus, the full-length K-Ras4B$_{1\text{-}188}$-GTP-γ-S interacted with Raf-1 RBD with higher efficiency than with truncated K-Ras4B$_{1\text{-}166}$-GTP-γ-S ($p < 0.001$). The interaction of Raf-1 RBD with full-length K-Ras4B$_{1\text{-}188}$-GDP was less efficient than with truncated K-Ras4B$_{1\text{-}166}$-GDP ($p < 0.001$). (*B*) MANT-GDP-bound recombinant truncated K-Ras4B$_{1\text{-}166}$ (0.3 μM) was incubated with 200 μM GDP in the presence of 0.6 μM SOS1. The rate of fluorescence decrease was slower in the presence of HVR analog (*red*) compared to the control (*black*), but inhibition of exchange appeared incomplete when compared to the rate of uncatalyzed exchange (*blue*). To see this figure in color, go online.

role in fencing off premature signaling from the GDP-bound protein. At the same time, the presence of HVR in full-length K-Ras4B-GTP-γ-S increases the interaction efficiency with Raf RBD, implying that there is a possible binding site for HVR in Raf. Thus, HVR in both the sequestered and released conformations can regulate signaling through Raf, and other effectors, such as PI3K. Importantly, the HVR in K-Ras4B-GTP provides the major binding site for calmodulin (36); in the GDP-bound state, the HVR is unavailable to interact with calmodulin due to its sequestration by the catalytic domain.

It is difficult to speculate whether HVRs similarly autoinhibit other Ras GTPases. Ras isoforms differ predominantly in their HVR regions and these differences have functional implications (48,49). In H-Ras, the HVR affects backbone dynamics of the catalytic domain. However, high affinity sequestration was not observed (50). HVRs of other Ras isoforms may also regulate effector binding and/or GDP/GTP exchange. Domain swapping has shown that H-Ras, but not N-Ras HVR, determines the invasive/migratory signaling program in breast tumor cells, independent of differences in lipidation between the two HVRs (51).

It is also unclear whether the newly discovered autoinhibition mechanism plays a role in K-Ras-mediated oncogenesis. Our finding that an oncogenic mutation in K-Ras affects the interaction of HVR with the active site allows us to speculate that oncogenic mutations may allosterically

modulate HVR-binding affinity. Our recent results suggest that this is indeed the case, at least for those mutations that we inspected, i.e., G12C, G12D, G12V, G13D, Q61H, and R164Q, and for E37K orthosterically (52). This particularly holds for GTP-bound K-Ras4B.

The role of HVR in K-Ras4B-induced oncogenesis remains controversial, with reports supporting both highly significant and more subtle effects of HVR mutations on K-Ras4B G12V-dependent cancer transformation (18,53). Detailed studies of HVR interactions in different Ras mutants may uncover additional modes of modulation of oncogenic activity.

Finally, the high affinity interaction of HVR with the active site of K-Ras4B suggests that targeting this surface with synthetic inhibitors is feasible. Optimization of compounds that bind at the HVR-catalytic domain interface and promote K-Ras4B autoinhibition is a potentially promising approach for development of potent inhibitors of so-far undruggable Ras (12). However, drug resistance may still be expected to arise and a combinatorial drug cocktail regime (13) will still be required.

SUPPORTING MATERIAL

Ten figures are available at http://www.biophysj.org/biophysj/supplemental/S0006-3495(15)01104-2.

AUTHOR CONTRIBUTIONS

T.S.C., H.J., L.K., V.G., R.N., and N.I.T. conceived and designed the study; T.S.C., S.J.A., A.B., and V.G. performed NMR experiments; L.K., B.C.F., L.J., S.G.T., and N.I.T. performed MST and peptide binding experiments; H.J. and R.N. performed MD simulations; T.S.C., H.J., L.K., V.G., R.N., and N.I.T. prepared and wrote the article; and all authors edited and approved the article.

ACKNOWLEDGMENTS

The content of this publication does not necessarily reflect the views or policies of the Department of Health and Human Services, nor does mention of trade names, commercial products or organizations imply endorsement by the US Government.

All simulations had been performed using the high-performance computational facilities of the Biowulf PC/Linux cluster at the National Institutes of Health, Bethesda, MD (http://biowulf.nih.gov).

We gratefully acknowledge the generous support from the National Cancer Institute (Awards R01CA135341 and R01CA188427); the National Heart, Lung, and Blood Institute (Award R21HL118588); and the National Institute of Allergy and Infectious Diseases (Award R01AI058072) to V.G. This project has been funded in whole or in part with federal funds from the Frederick National Laboratory for Cancer Research, National Institutes of Health, under contract No. HHSN261200800001E. This research was supported (in part) by the Intramural Research Program of the National Institutes of Health, Frederick National Lab, Center for Cancer Research.

SUPPORTING CITATIONS

References (54-56) appear in the Supporting Material.

REFERENCES

1. Karnoub, A. E., and R. A. Weinberg. 2008. Ras oncogenes: split personalities. *Nat. Rev. Mol. Cell Biol.* 9:517–531.
2. Pleasance, E. D., R. K. Cheetham, …, M. R. Stratton. 2010. A comprehensive catalogue of somatic mutations from a human cancer genome. *Nature.* 463:191–196.
3. Prior, I. A., P. D. Lewis, and C. Mattos. 2012. A comprehensive survey of Ras mutations in cancer. *Cancer Res.* 72:2457–2467.
4. Stephen, A. G., D. Esposito, …, F. McCormick. 2014. Dragging Ras back in the ring. *Cancer Cell.* 25:272–281.
5. Schlichting, I., S. C. Almo, …, R. S. Goody. 1990. Time-resolved x-ray crystallographic study of the conformational change in Ha-Ras p21 protein on GTP hydrolysis. *Nature.* 345:309–315.
6. Scheffzek, K., M. R. Ahmadian, …, A. Wittinghofer. 1997. The Ras-RasGAP complex: structural basis for GTPase activation and its loss in oncogenic Ras mutants. *Science.* 277:333–338.
7. Wittinghofer, A., and I. R. Vetter. 2011. Structure-function relationships of the G domain, a canonical switch motif. *Annu. Rev. Biochem.* 80:943–971.
8. Saxena, N., S. S. Lahiri, …, R. P. Tripathi. 2008. RAS: target for cancer therapy. *Cancer Invest.* 26:948–955.
9. Maurer, T., L. S. Garrenton, …, G. Fang. 2012. Small-molecule ligands bind to a distinct pocket in Ras and inhibit SOS-mediated nucleotide exchange activity. *Proc. Natl. Acad. Sci. USA.* 109:5299–5304.
10. Ostrem, J. M., U. Peters, …, K. M. Shokat. 2013. K-Ras(G12C) inhibitors allosterically control GTP affinity and effector interactions. *Nature.* 503:548–551.
11. Sun, Q., J. P. Burke, …, S. W. Fesik. 2012. Discovery of small molecules that bind to K-Ras and inhibit Sos-mediated activation. *Angew. Chem. Int.Engl.* 51:6140–6143.
12. Wang, W., G. Fang, and J. Rudolph. 2012. Ras inhibition via direct Ras binding—is there a path forward? *Bioorg. Med. Chem. Lett.* 22:5766–5776.
13. Nussinov, R., C. J. Tsai, and C. Mattos. 2013. 'Pathway drug cocktail': targeting Ras signaling based on structural pathways. *Trends Mol. Med.* 19:695–704.
14. Gysin, S., M. Salt, …, F. McCormick. 2011. Therapeutic strategies for targeting Ras proteins. *Genes Cancer.* 2:359–372.
15. Thompson, H. 2013. US National Cancer Institute's new Ras project targets an old foe. *Nat. Med.* 19:949–950.
16. Iwig, J. S., and J. Kuriyan. 2013. Fixing a hole where the Ras gets in. *Cell.* 153:1191–1193.
17. Resh, M. D. 2004. Membrane targeting of lipid modified signal transduction proteins. *Subcell. Biochem.* 37:217–232.
18. Hancock, J. F., H. Paterson, and C. J. Marshall. 1990. A polybasic domain or palmitoylation is required in addition to the CAAX motif to localize p21ras to the plasma membrane. *Cell.* 63:133–139.
19. Ahearn, I. M., K. Haigis, …, M. R. Philips. 2012. Regulating the regulator: post-translational modification of RAS. *Nat. Rev. Mol. Cell Biol.* 13:39–51.
20. Abankwa, D., A. A. Gorfe, …, J. F. Hancock. 2010. Ras membrane orientation and nanodomain localization generate isoform diversity. *Proc. Natl. Acad. Sci. USA.* 107:1130–1135.
21. Quinlan, M. P., and J. Settleman. 2009. Isoform-specific Ras functions in development and cancer. *Future Oncol.* 5:105–116.
22. Castellano, E., and E. Santos. 2011. Functional specificity of Ras isoforms: so similar but so different. *Genes Cancer.* 2:216–231.
23. Jang, H., S. J. Abraham, …, V. Gaponenko. 2015. Mechanisms of membrane binding of small GTPase K-Ras4B farnesylated hypervariable region. *J. Biol. Chem.* 290:9465–9477.
24. Milburn, M. V., L. Tong, …, S. H. Kim. 1990. Molecular switch for signal transduction: structural differences between active and inactive forms of protooncogenic Ras proteins. *Science.* 247:939–945.

25. Akimoto, M., R. Selvaratnam, …, G. Melacini. 2013. Signaling through dynamic linkers as revealed by PKA. *Proc. Natl. Acad. Sci. USA.* 110:14231–14236.

26. Johannessen, L., J. Remsberg, …, N. I. Tarasova. 2011. Peptide structure stabilization by membrane anchoring and its general applicability to the development of potent cell-permeable inhibitors. *ChemBioChem.* 12:914–921.

27. Abraham, S. J., I. Muhamed, …, V. Gaponenko. 2010. Expression, purification, and characterization of soluble K-Ras4B for structural analysis. *Protein Expr. Purif.* 73:125–131.

28. Neidhardt, F. C., P. L. Bloch, and D. F. Smith. 1974. Culture medium for enterobacteria. *J. Bacteriol.* 119:736–747.

29. Delaglio, F., S. Grzesiek, …, A. Bax. 1995. NMRPipe: a multidimensional spectral processing system based on UNIX pipes. *J. Biomol. NMR.* 6:277–293.

30. Brooks, B. R., R. E. Bruccoleri, …, M. Karplus. 1983. CHARMM—a program for macromolecular energy, minimization, and dynamics calculations. *J. Comput. Chem.* 4:187–217.

31. Grayson, P., E. Tajkhorshid, and K. Schulten. 2003. Mechanisms of selectivity in channels and enzymes studied with interactive molecular dynamics. *Biophys. J.* 85:36–48.

32. Humphrey, W., A. Dalke, and K. Schulten. 1996. VMD: visual molecular dynamics. *J. Mol. Graph.* 14:27–38.

33. Phillips, J. C., R. Braun, …, K. Schulten. 2005. Scalable molecular dynamics with NAMD. *J. Comput. Chem.* 26:1781–1802.

34. Durell, S. R., B. R. Brooks, and A. Bennaim. 1994. Solvent-induced forces between two hydrophilic groups. *J. Phys. Chem.* 98:2198–2202.

35. Chavan, T. S., J. O. Meyer, …, V. Gaponenko. 2014. A novel method for the production of fully modified K-Ras 4B. *Methods Mol. Biol.* 1120:19–32.

36. Abraham, S. J., R. P. Nolet, …, V. Gaponenko. 2009. The hypervariable region of K-Ras4B is responsible for its specific interactions with calmodulin. *Biochemistry.* 48:7575–7583.

37. Jerabek-Willemsen, M., C. J. Wienken, …, S. Duhr. 2011. Molecular interaction studies using microscale thermophoresis. *Assay Drug Dev. Technol.* 9:342–353.

38. Seidel, S. A., P. M. Dijkman, …, S. Duhr. 2013. Microscale thermophoresis quantifies biomolecular interactions under previously challenging conditions. *Methods.* 59:301–315.

39. Alvarez-Moya, B., C. Barceló, …, N. Agell. 2011. CaM interaction and Ser^{181} phosphorylation as new K-Ras signaling modulators. *Small GTPases.* 2:99–103.

40. Das, R., V. Esposito, …, G. Melacini. 2007. cAMP activation of PKA defines an ancient signaling mechanism. *Proc. Natl. Acad. Sci. USA.* 104:93–98.

41. Masterson, L. R., A. Mascioni, …, G. Veglia. 2008. Allosteric cooperativity in protein kinase A. *Proc. Natl. Acad. Sci. USA.* 105:506–511.

42. Herrmann, C., G. A. Martin, and A. Wittinghofer. 1995. Quantitative analysis of the complex between p21ras and the Ras-binding domain of the human Raf-1 protein kinase. *J. Biol. Chem.* 270:2901–2905.

43. Williams, J. G., J. K. Drugan, …, S. L. Campbell. 2000. Elucidation of binding determinants and functional consequences of Ras/Raf-cysteine-rich domain interactions. *J. Biol. Chem.* 275:22172–22179.

44. Boguski, M. S., and F. McCormick. 1993. Proteins regulating Ras and its relatives. *Nature.* 366:643–654.

45. Smith, M. J., and M. Ikura. 2014. Integrated RAS signaling defined by parallel NMR detection of effectors and regulators. *Nat. Chem. Biol.* 10:223–230.

46. Randazzo, P. A., T. Terui, …, R. A. Kahn. 1995. The myristoylated amino terminus of ADP-ribosylation factor 1 is a phospholipid- and GTP-sensitive switch. *J. Biol. Chem.* 270:14809–14815.

47. Ugolev, Y., Y. Berdichevsky, …, E. Pick. 2008. Dissociation of Rac1(GDP)•RhoGDI complexes by the cooperative action of anionic liposomes containing phosphatidylinositol 3,4,5-trisphosphate, Rac guanine nucleotide exchange factor, and GTP. *J. Biol. Chem.* 283:22257–22271.

48. Yan, J., S. Roy, …, J. F. Hancock. 1998. Ras isoforms vary in their ability to activate Raf-1 and phosphoinositide 3-kinase. *J. Biol. Chem.* 273:24052–24056.

49. Jones, M. K., and J. H. Jackson. 1998. Ras-GRF activates Ha-Ras, but not N-Ras or K-Ras 4B, protein in vivo. *J. Biol. Chem.* 273:1782–1787.

50. Thapar, R., J. G. Williams, and S. L. Campbell. 2004. NMR characterization of full-length farnesylated and non-farnesylated H-Ras and its implications for Raf activation. *J. Mol. Biol.* 343:1391–1408.

51. Yong, H. Y., J. S. Hwang, …, A. Moon. 2011. Identification of H-Ras-specific motif for the activation of invasive signaling program in human breast epithelial cells. *Neoplasia.* 13:98–107.

52. Lu, S., A. Banerjee, …, R. Nussinov. 2015. GTP binding and oncogenic mutations may attenuate hypervariable region (HVR)-catalytic domain interactions in small GTPase KRAS4B, exposing the effector finding site. *J. Biol. Chem.* Published online October 9, 2015. http://dx.doi.org/10.1074/jbc.M115.664755.

53. Jackson, J. H., J. W. Li, …, C. G. Cochrane. 1994. Polylysine domain of K-ras 4B protein is crucial for malignant transformation. *Proc. Natl. Acad. Sci. USA.* 91:12730–12734.

54. Frishman, D., and P. Argos. 1995. Knowledge-based protein secondary structure assignment. *Proteins.* 23:566–579.

55. Neal, S., A. M. Nip, …, D. S. Wishart. 2003. Rapid and accurate calculation of protein ^{1}H, ^{13}C and ^{15}N chemical shifts. *J. Biomol. NMR.* 26:215–240.

56. Tochio, H., F. Hung, …, M. Zhang. 2000. Solution structure and backbone dynamics of the second PDZ domain of postsynaptic density-95. *J. Mol. Biol.* 295:225–237.

Supporting Material

High Affinity Interaction of K-Ras4B Hypervariable Region with Ras Active Site

Tanmay S. Chavan,[1,2] Hyunbum Jang,[3,4] Lyuba Khavrutskii,[3,4] Sherwin J. Abraham,[2] Avik Banerjee,[5] Benjamin C. Freed,[4] Liv Johannessen,[4] Sergey G. Tarasov,[5] Vadim Gaponenko,*[,2] Ruth Nussinov,*[,3,4,6] and Nadya I. Tarasova*[,3]

Departments of [1]Medicinal Chemistry, [2]Biochemistry and Molecular Genetics, and [5]Chemistry, University of Illinois at Chicago, Chicago, IL 60607, U.S.A.
[3]Basic Science Program, Leidos Biomedical Research, Inc., Frederick National Laboratory for Cancer Research, [4]Cancer and Inflammation Program, [5]Structural Biophysics Laboratory, National Cancer Institute at Frederick, Frederick, MD 21702, U.S.A.
[6]Department of Human Molecular Genetics and Biochemistry, Sackler School of Medicine, Tel Aviv University, Tel Aviv 69978, Israel

Figure S1

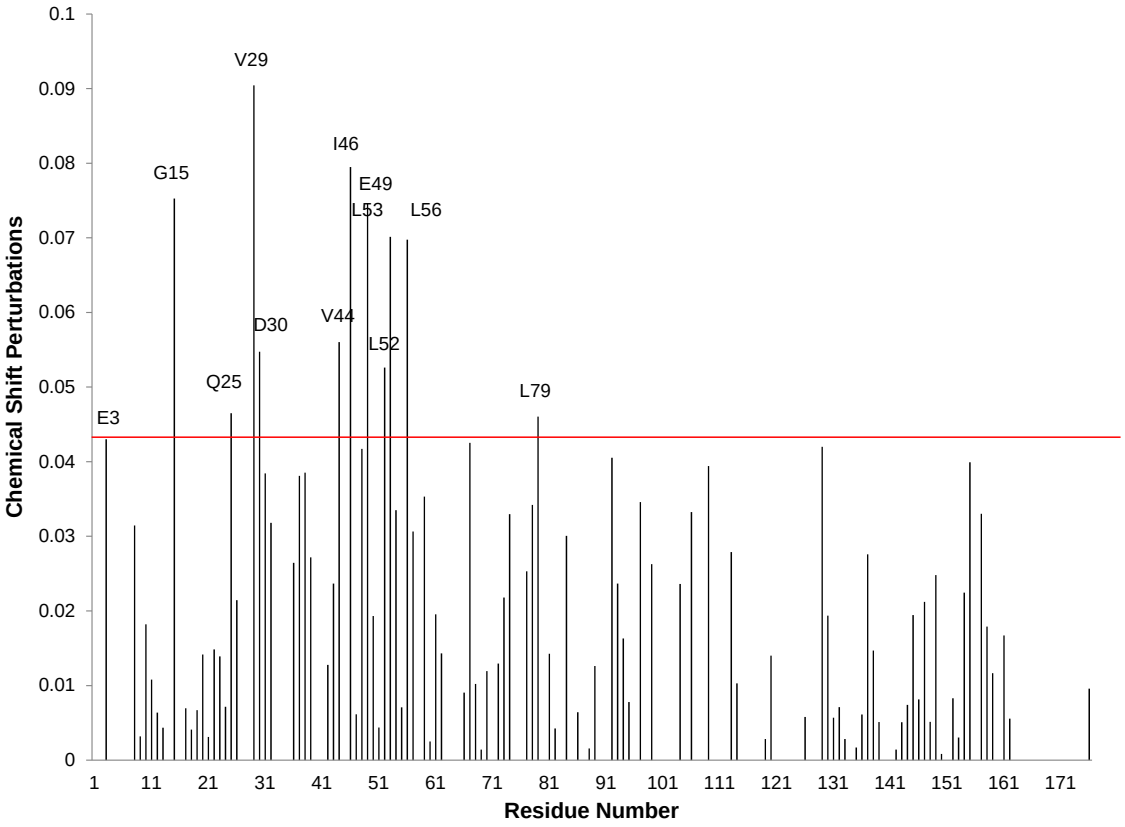

Figure S1 Chemical shift perturbations (CSPs) in K175A mutant. The K175A mutation in the HVR causes CSPs in the catalytic domain of K-Ras4B-GDP. Chemical shift changes obtained after overlaying ^{15}N-HSQC NMR spectra of wild-type K-Ras4B-GDP and K175A mutant of K-Ras4B-GDP. The red horizontal line in the graph shows the sum of average CSP and one standard deviation. The names of residues exhibiting statistically significant (above the line) CSPs are marked.

Figure S2

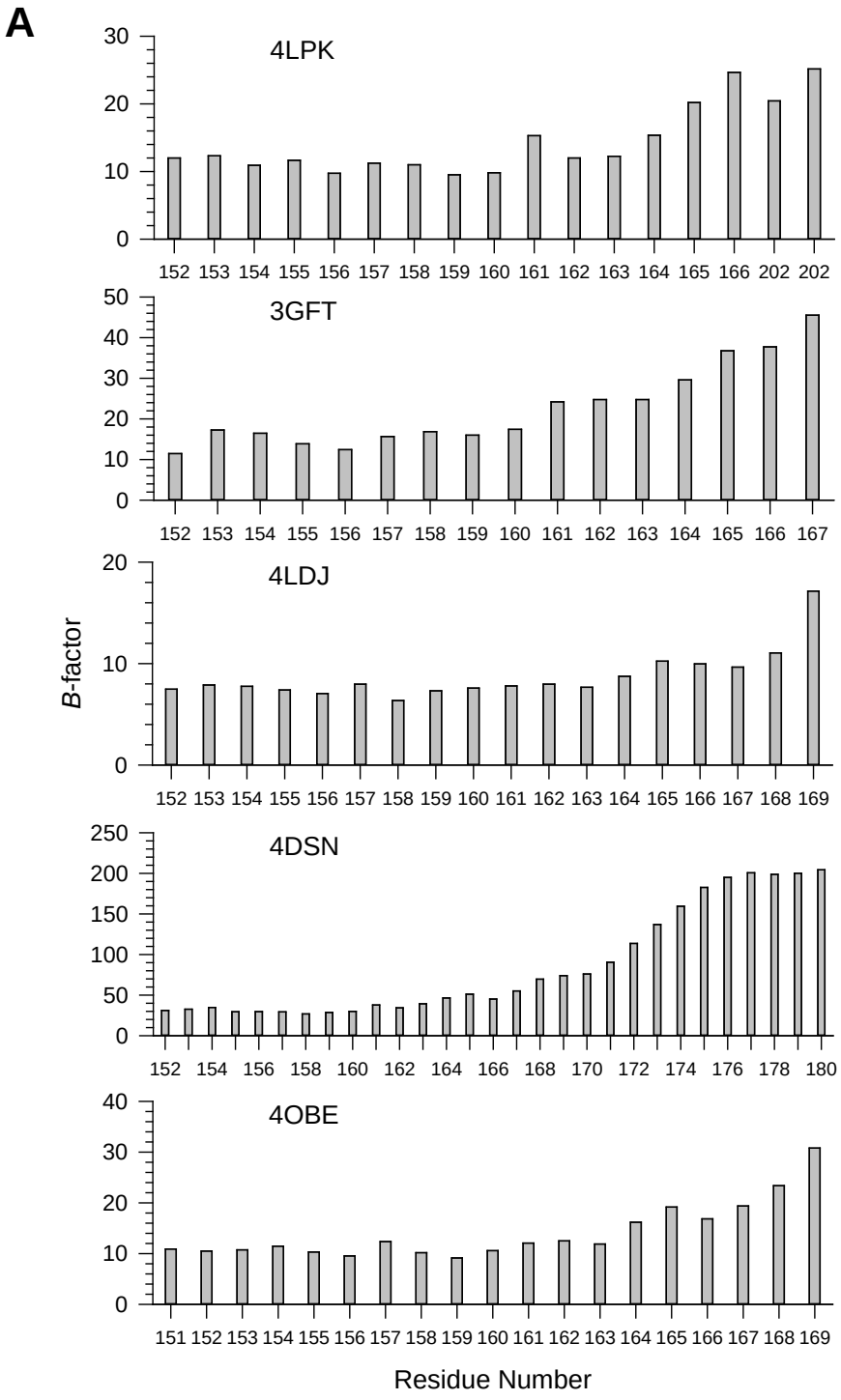

Figure S2 The temperature factors (*B*-factors) of the corresponding residues of selected K-Ras4B crystal structures; wild-type K-Ras4B-GDP (PDB code: 4LPK), Q61H K-Ras4B-GTP (PDB code: 3GFT), G12C K-Ras4B-GDP (PDB code: 4LDJ), G12D K-Ras4B-GTP (PDB code: 4DSN), and wild-type K-Ras4B-GDP (PDB code: 4OBE).

Figure S3

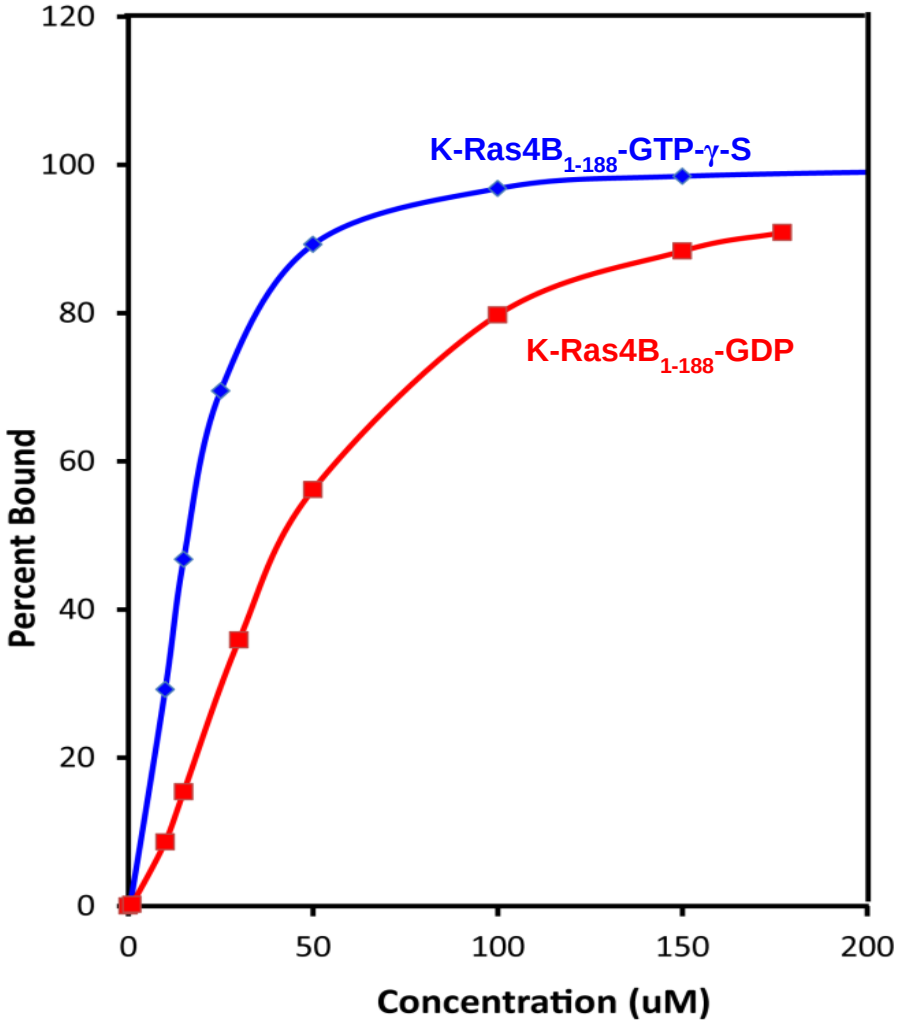

Figure S3 K-Ras4B-GTP-γ-S has a higher affinity for phospholipid bilayers than K-Ras4B-GDP. To test the effect of HVR sequestration in the GDP-bound form on the interaction with the plasma membrane phospholipids, we performed a surface plasmon resonance (SPR) membrane binding assay on the GDP- and GTP-loaded K-Ras4B$_{1\text{-}188}$ (1). Different concentrations of either K-Ras4B$_{1\text{-}188}$-GDP or K-Ras4B$_{1\text{-}188}$-GTP-γ-S were individually titrated onto dipalmitoyl phosphatidyl choline nanodiscs immobilized on a CM5 sensor chip. Non-linear regression fits on the data points revealed that there is almost a 5-fold decrease in affinity for the nanodiscs when the protein is GDP-bound as compared to when it is GTP-γ-S-bound. The apparent K_D for K-Ras4B-GDP is 107.2 ± 6 μM, while K-Ras4B-GTP-γ-S has an apparent K_D of 24.0 ± 2 μM for DPPC nanodiscs. These values reflect the HVR-mediated binding to phospholipids. The membrane binding affinity may be higher when K-Ras4B is post-translationally lipidated and carboxymethylated. Our results suggest that the HVR sequestration in the GDP-bound state lowers the membrane binding affinity, while its release in the GTP-bound state allows for tighter association with phospholipids.

Figure S4

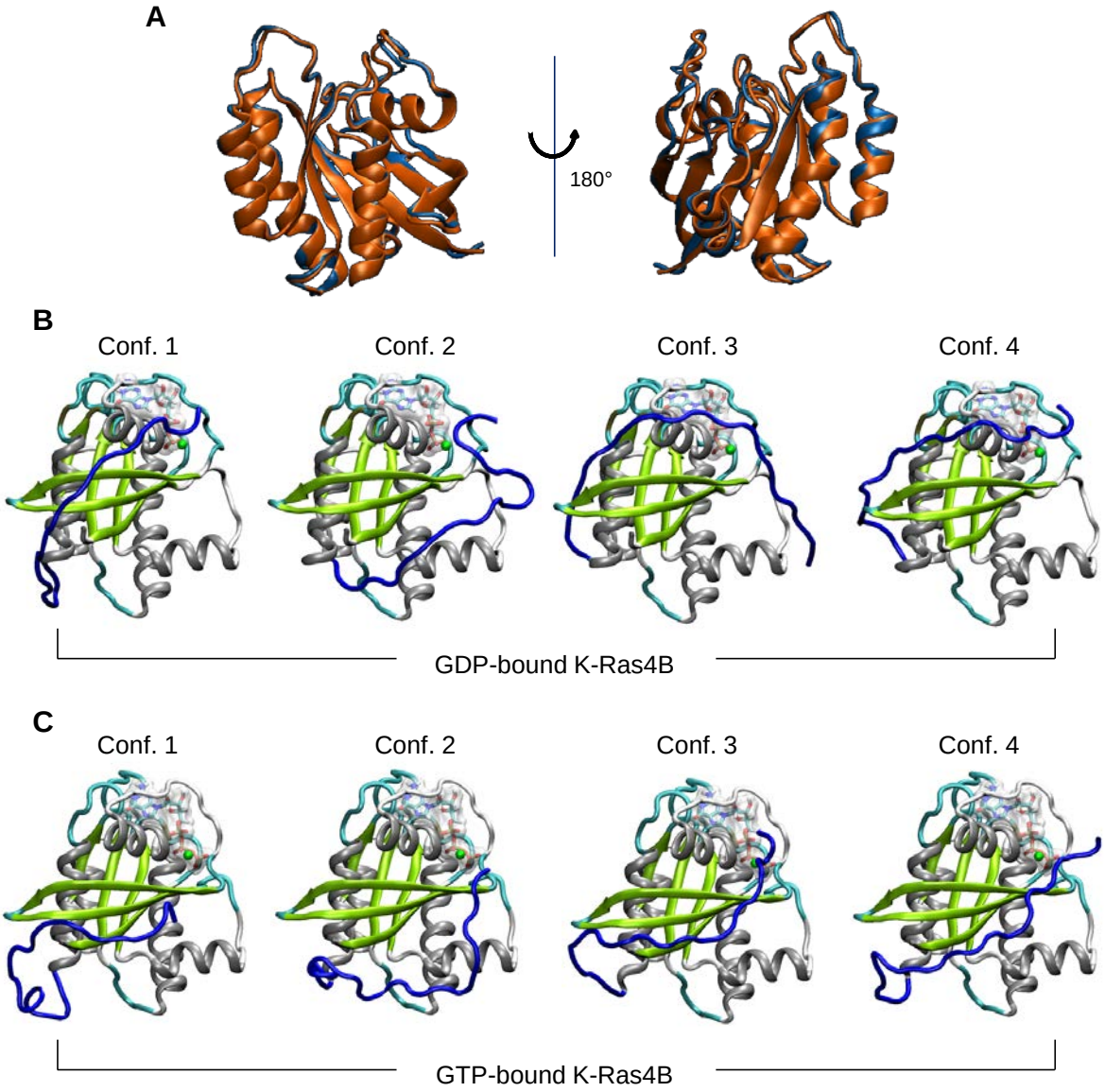

Figure S4 Ras crystal structures with residues 1-166 and initial configurations of full-length K-Ras4B proteins for the molecular dynamics (MD) simulations based on the crystal structures and NMR data. (*A*) Superimposition of the crystal structures for the GDP-bound (PDB code: 4EPT, light blue) and GTP-bound (PDB code: 3GFT, orange) K-Ras4B$_{1\text{-}166}$. For the full-length K-Ras4B with HVR, initial coordinates of the catalytic domain were taken from the Ras crystal structures representing the (*B*) GDP-bound and (*C*) GTP-bound states of K-Ras4B. The covalently connected HVRs were modeled and folded onto the catalytic domain using the interactive molecular dynamics (IMD) (2). The initial locations of the HVR were based on the NMR chemical shift perturbations. In the catalytic domain, the α-helix and β-sheet secondary structures are colored gray and yellow, respectively, and the HVR is colored blue.

Figure S5

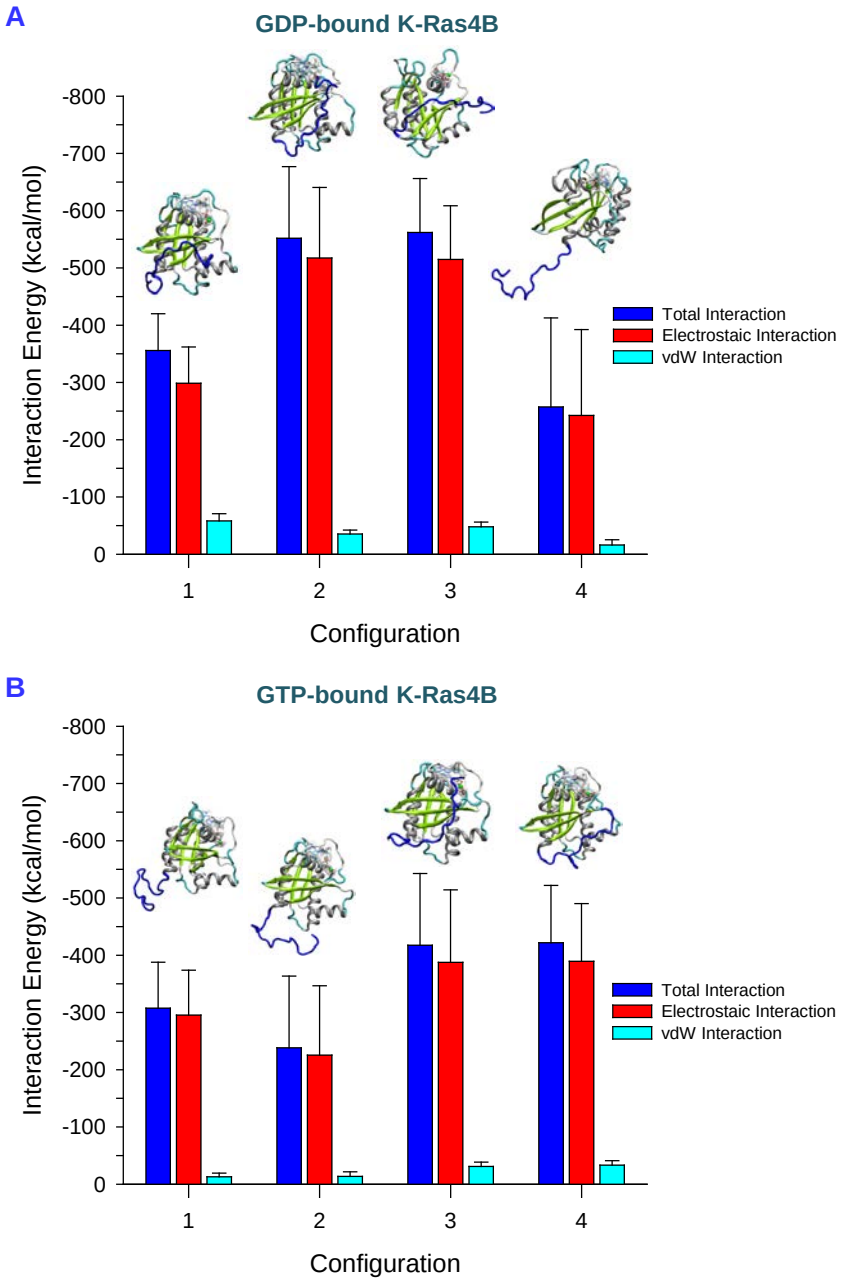

Figure S5 Interaction energy of the HVR with K-Ras4B catalytic domain. Averaged total interaction energy (blue bars) of HVR with the catalytic domain, and the contributions from the electrostatic (red bars) and vdW (cyan bars) interactions for four different configurations of K-Ras4B in the (*A*) GDP-bound and (*B*) GTP-bound states. Averaged protein structures are embedded on the corresponding configuration bars. Interactions of HVR with the catalytic domain are mainly driven by electrostatics and reveal stronger attraction in GDP-K-Ras4B as compared to the GTP counterpart. Based on these data, we designated the configurations 2 and 3 of K-Ras4B-GDP and the configurations 3 and 4 of K-Ras4B-GTP for the best model conformations of HVR interacting with the catalytic domain.

Figure S6

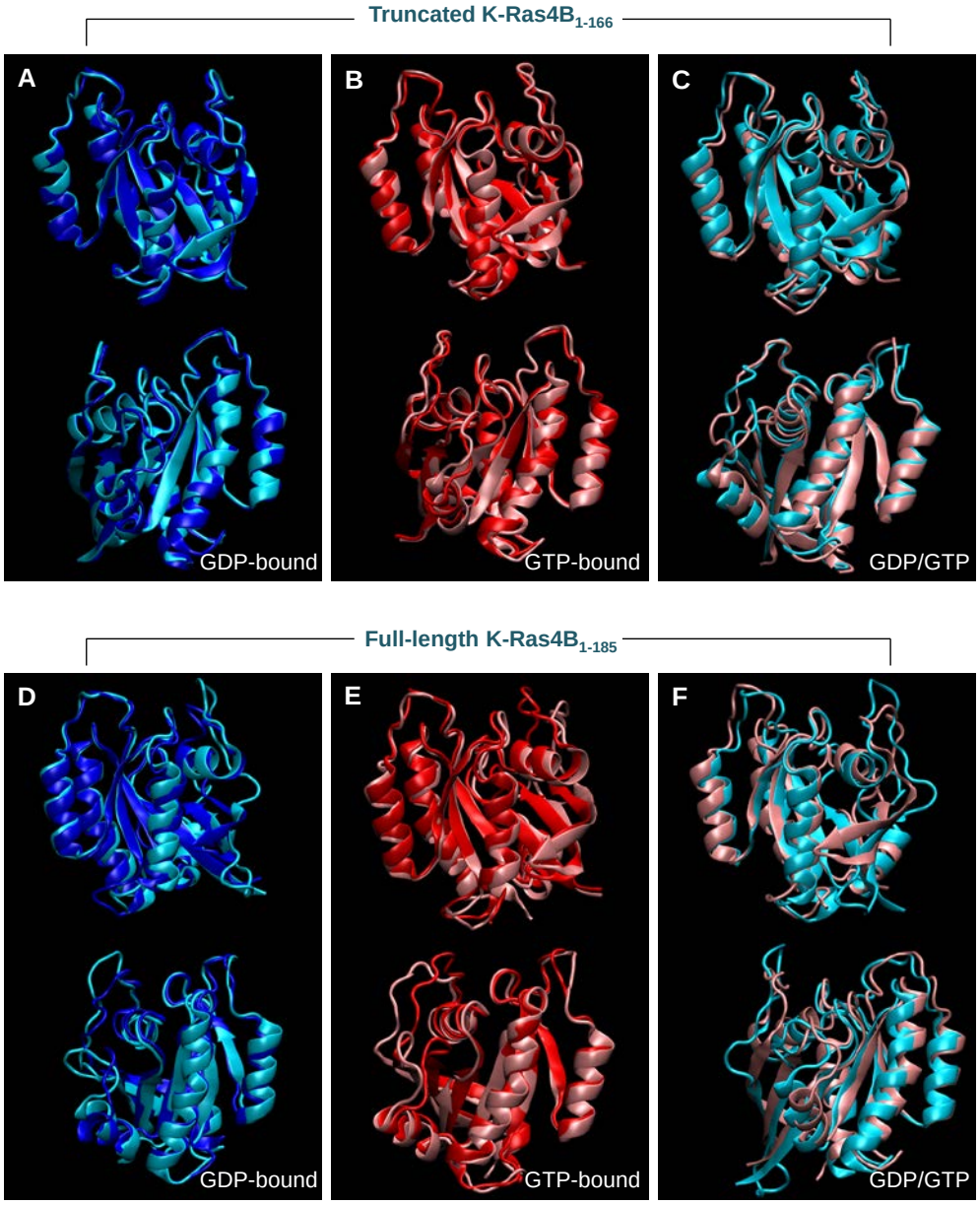

Figure S6 Conformational changes in the catalytic domain. Small changes have been detected in the truncated K-Ras4B, but large structural differences can be observed in the full-length protein. Superimpositions of the starting points (blue and red) with the relaxed structures (cyan and pink) obtained from the simulations for K-Ras4B$_{1\text{-}166}$ in the (*A*) GDP-bound and (*B*) GTP-bound states. (*C*) Superimpositions between those relaxed structures in the GDP-bound (cyan) and GTP-bound (pink) K-Ras4B$_{1\text{-}166}$ after the simulations. Superimpositions of the starting points (blue and red) with the relaxed structures (cyan and pink) obtained from the simulations for K-Ras4B$_{1\text{-}185}$ in the (*D*) GDP-bound (config. 3) and (*E*) GTP-bound (config. 3) states. (*F*) Superimpositions between those relaxed structures in the GDP-bound (cyan, config. 3) and GTP-bound (pink, config. 3) K-Ras4B$_{1\text{-}185}$ after the simulations. For clarity, the HVR is removed.

Figure S7

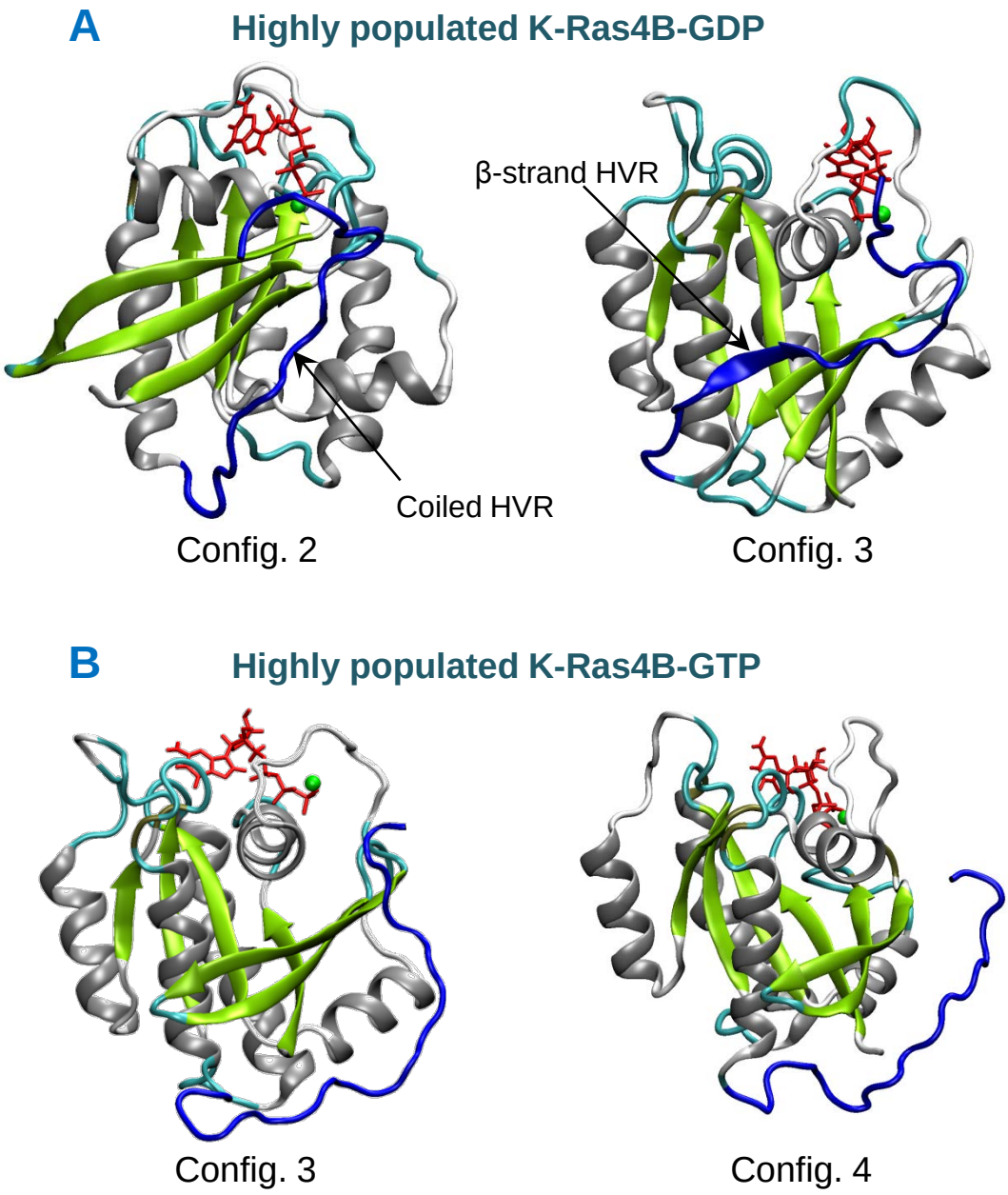

Figure S7 Molecular structures of highly populated full-length K-Ras4B are shown in the (*A*) GDP-bound and (*B*) GTP-bound states from molecular dynamics (MD) simulations. The cartoons depict snapshots of the protein conformations for configurations 2 and 3 K-Ras4B-GDP and for configurations 3 and 4 K-Ras4B-GTP at t = 100 ns (see Figs. 6 and S4). In the catalytic domain, the α-helix and β-sheet secondary structures are colored gray and yellow, respectively, and the HVR is colored blue.

Figure S8

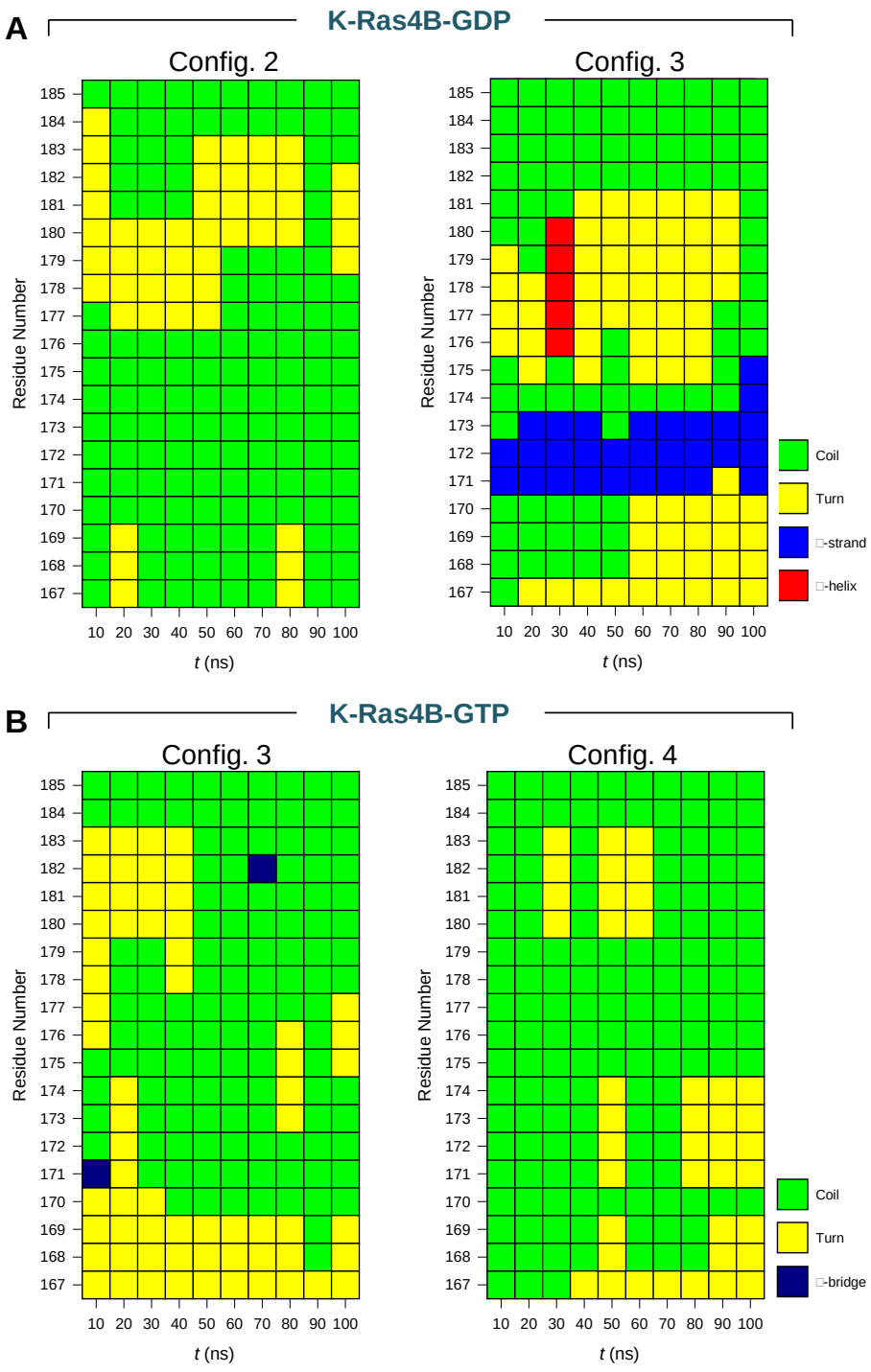

Figure S8 Investigation of the secondary structure for the HVR of K-Ras4B. Descriptions of the HVR secondary structure by STRIDE (3) averaged over each 10 ns interval for (*A*) configurations 2 (left panel) and 3 (right panel) K-Ras4B-GDP, and (*B*) configurations 3 (left panel) and 4 (right panel) K-Ras4B-GTP.

Figure S9

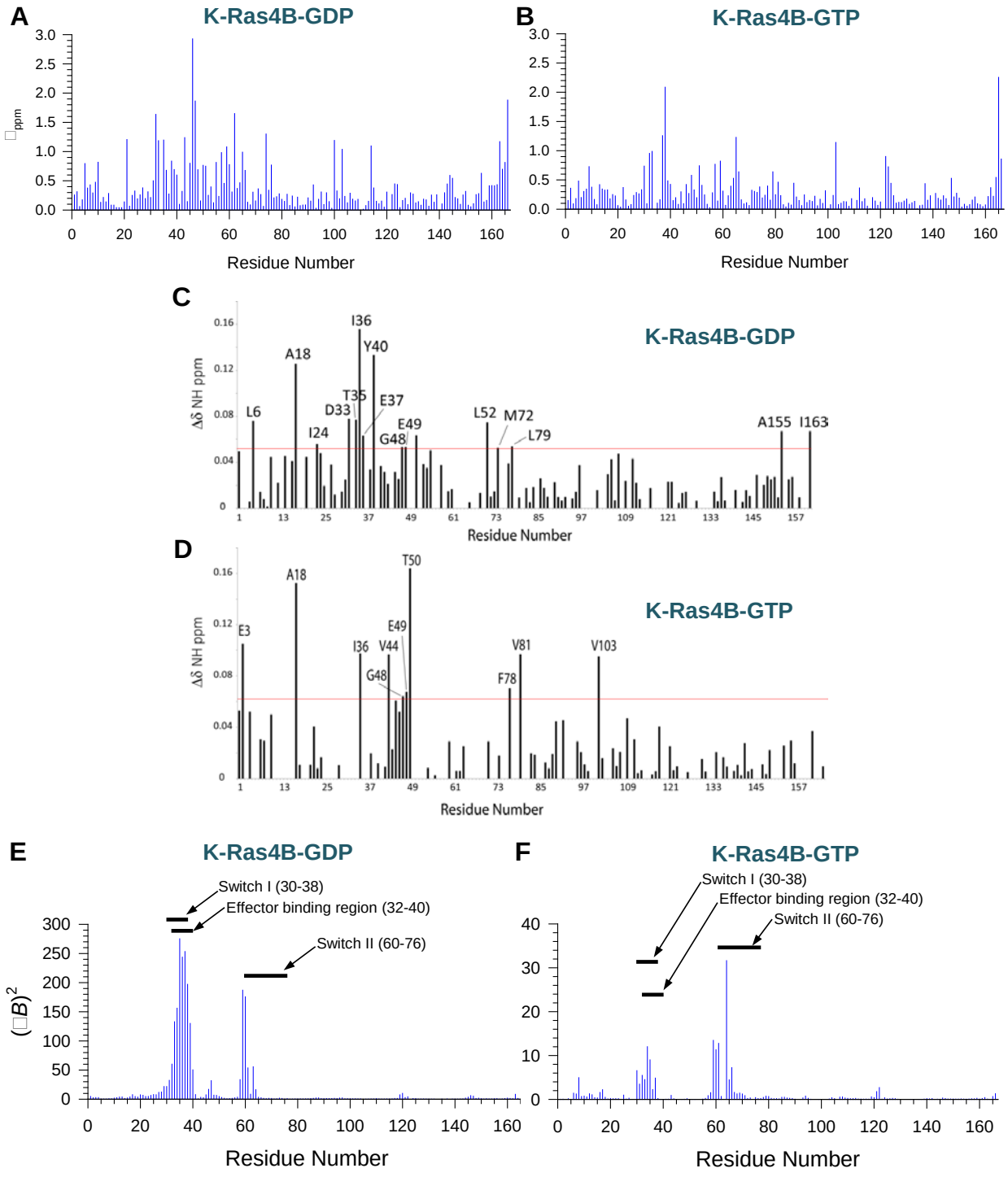

Figure S9 Comparisons of theoretical estimations of the chemical shift perturbations (CSPs) with the NMR CSPs. The combined CSPs using the ShiftX (4) program was used to calculate ^{1}H, ^{13}C, and ^{15}N chemical shifts. The combined CSPs for the full-length K-Ras4B with respect to K-Ras4B$_{1\text{-}166}$ during the simulations were calculated using the equation (5) $\Delta_{ppm}=$

$\sqrt{(\Delta\delta_{HN})^2 + (\Delta\delta_N\alpha_N)^2}$, where α_N is a scaling factor with a value 0.17, for the (*A*) GDP-bound and (*B*) GTP-bound K-Ras4B. Exemples represented here for both configurations 3 of GDP- and GTP-bound states. Residual chemical shifts obtained after the overlay of ^{15}N HSQC NMR spectra of (*C*) full length K-Ras4B-GDP and that of K-Ras4B$_{1\text{-}166}$-GDP, and of (*D*) full length K-Ras4B-GTP-γ-S and that of K-Ras4B$_{1\text{-}166}$-GTP-γ-S. The horizontal line in the graph shows the sum of average CSP and standard deviation. Residues that show zero chemical shift difference on the graph were the ones that were not assigned due to resonance overlap. Perturbations of the temperature factor (*B*-factor) indicate largest changes upon HVR binding to GDP-bound K-Ras4B in the residues on β2, including the effector binding region and Switch I and II. The *B*-factors from the catalytic domain RMSF in the full-length K-Ras4B were subtracted by those from the control simulations of truncated K-Ras4B$_{1\text{-}166}$ at each frame, and then squared for the (*E*) GDP-bound and (*F*) GTP-bound states. Exemples represented here for both configurations 3 of GDP- and GTP-bound states.

Figure S10

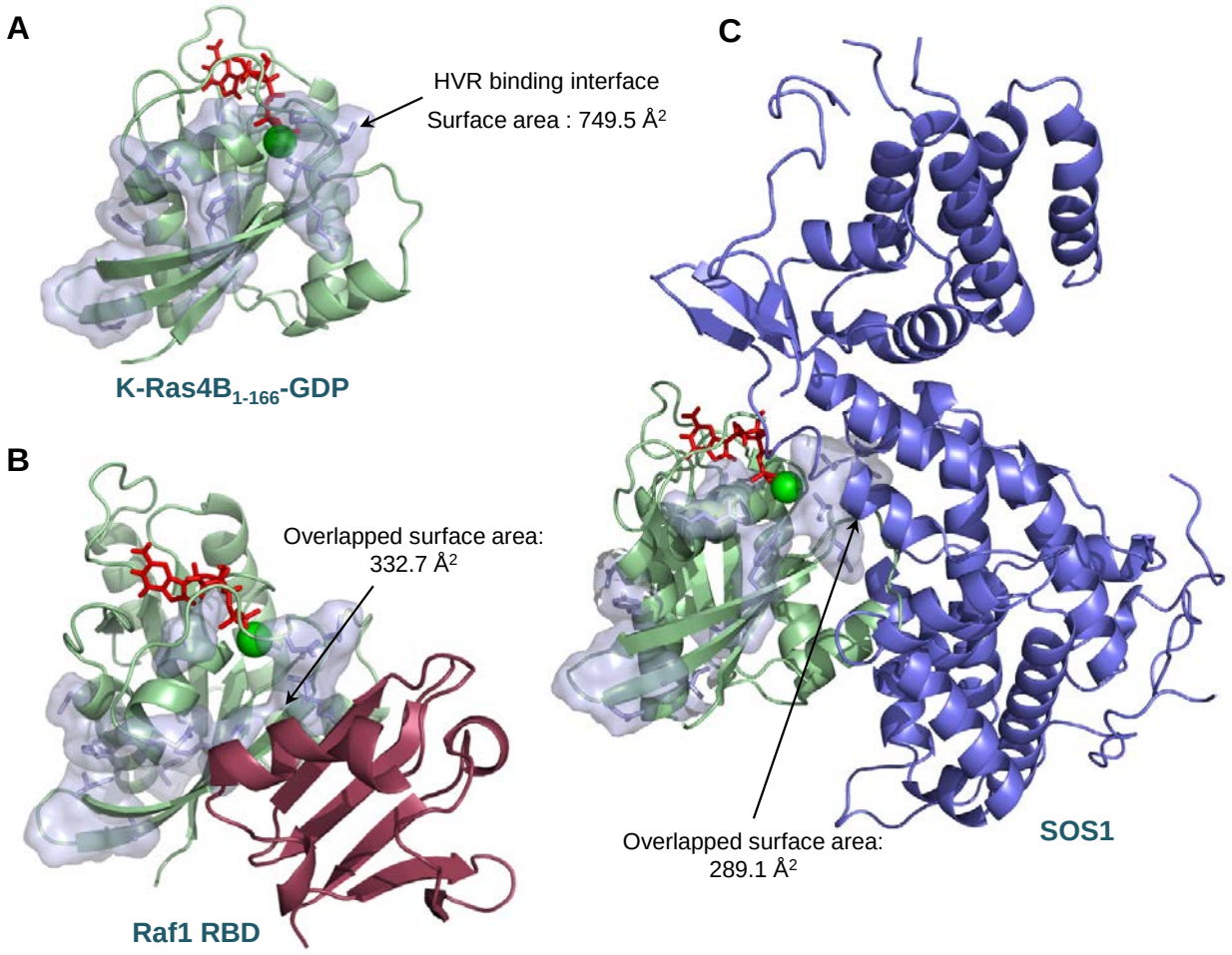

Figure S10 The overlap in the HVR binding interface of K-Ras4B with that of GEFs is significantly lesser than with Raf. (*A*) Structure of K-Ras4B$_{1-166}$-GDP protein with highlighted the HVR binding interface in surface representation. Surface area of the HVR binding interface is 749.5 Å^2. (*B*) Modeled dimer structure of K-Ras4B$_{1-166}$-GDP with Ras-binding-domain (RBD) of Raf1. The dimer structure was reconstituted from the X-ray crystal structure of the complex between the Ras-related protein Rap1A in the GTP-analogue (GppNHp) form and the RBD of Raf1 (PDB code: 1C1Y). Overlapped surface area in the HVR binding interface by the RBD of Raf1 is 332.7 Å^2. (*C*) Modeled complex structure of K-Ras4B$_{1-166}$-GDP with the Ras guanine-nucleotide-exchange-factor (GEF) region of the son of sevenless-1 (SOS-1). The K-Ras4B/SOS-1 structure was reconstituted from the crystal structure of human H-Ras/SOS-1 complex (PDB code: 1BKD). Overlapped surface area in the HVR binding interface by the SOS-1 is 289.1 Å^2.

Supporting References

1. Chavan, T. S., J. O. Meyer, L. Chisholm, M. Dobosz-Bartoszek, and V. Gaponenko. 2014. A novel method for the production of fully modified K-Ras 4B. Methods Mol Biol 1120:19-32.
2. Grayson, P., E. Tajkhorshid, and K. Schulten. 2003. Mechanisms of selectivity in channels and enzymes studied with interactive molecular dynamics. Biophys J 85:36-48.
3. Frishman, D., and P. Argos. 1995. Knowledge-based protein secondary structure assignment. Proteins 23:566-579.
4. Neal, S., A. M. Nip, H. Zhang, and D. S. Wishart. 2003. Rapid and accurate calculation of protein 1H, 13C and 15N chemical shifts. J Biomol NMR 26:215-240.
5. Tochio, H., F. Hung, M. Li, D. S. Bredt, and M. Zhang. 2000. Solution structure and backbone dynamics of the second PDZ domain of postsynaptic density-95. J Mol Biol 295:225-237.